



HAL
open science

Distinct metabolic programs established in the thymus control effector functions of $\gamma\delta$ T cell subsets in tumor microenvironments

Noella Lopes, Claire McIntyre, Stefania Martin, Mathilde Raverdeau, Nital Sumaria, Ayano Kohlgruber, Gina Fiala, Leandro Agudelo, Lydia Dyck, Harry Kane, et al.

► To cite this version:

Noella Lopes, Claire McIntyre, Stefania Martin, Mathilde Raverdeau, Nital Sumaria, et al.. Distinct metabolic programs established in the thymus control effector functions of $\gamma\delta$ T cell subsets in tumor microenvironments. *Nature Immunology*, 2021, 22 (2), pp.179-192. 10.1038/s41590-020-00848-3 . hal-03121669

HAL Id: hal-03121669

<https://hal.science/hal-03121669v1>

Submitted on 28 Oct 2021

HAL is a multi-disciplinary open access archive for the deposit and dissemination of scientific research documents, whether they are published or not. The documents may come from teaching and research institutions in France or abroad, or from public or private research centers.

L'archive ouverte pluridisciplinaire **HAL**, est destinée au dépôt et à la diffusion de documents scientifiques de niveau recherche, publiés ou non, émanant des établissements d'enseignement et de recherche français ou étrangers, des laboratoires publics ou privés.

1
2
3
4
5
6
7
8
9
10
11
12
13
14
15
16
17
18
19
20
21
22
23
24
25
26
27
28
29

Distinct metabolic programmes established in the thymus control effector functions of $\gamma\delta$ T cell subsets in tumour microenvironments

Noella Lopes^{1,8}, Claire McIntyre^{2,8}, Stefania Martin^{3,8}, Mathilde Raverdeau^{4,8}, Nital Sumaria³, Ayano C. Kohlgruber², Gina J. Fiala¹, Leandro Agudelo⁵, Lydia Dyck⁴, Harry Kane^{2,4}, Aaron Douglas⁴, Stephen Cunningham⁴, Hannah Prendeville⁴, Roisin Loftus⁴, Colleen Carmody², Philippe Pierre^{5,6}, Manolis Kellis⁷, Michael Brenner², Rafael J. Argüello⁵, Bruno Silva-Santos^{1,9}, Daniel J. Pennington^{3,9} and Lydia Lynch^{2,4,9}

¹Instituto de Medicina Molecular João Lobo Antunes, Faculdade de Medicina, Universidade de Lisboa, Lisbon, Portugal.

²Brigham and Women's Hospital, Harvard Medical School, Boston MA, USA.

³Blizard Institute, Barts and The London School of Medicine, Queen Mary University of London, London, E1 2AT, UK.

⁴Trinity Biomedical Science Institute, Trinity College Dublin, Dublin, Ireland.

⁵Aix Marseille Université, CNRS, INSERM, CIML, Centre d'Immunologie de Marseille-Luminy, Marseille, France.

⁶Institute for Research in Biomedicine (iBiMED) and Ildio Pinho Foundation, Department of Medical Sciences, University of Aveiro, 3810-193 Aveiro, Portugal.

⁷MIT Computer Science and Artificial Intelligence Laboratory, MA, USA.

⁸ and ⁹ These authors contributed equally to this work.

Correspondence should be addressed to D.J.P. (d.pennington@qmul.ac.uk).

30 **Abstract**

31 Metabolic programming controls immune cell lineages and functions, but little
32 is known about $\gamma\delta$ T cell metabolism. Here, we found that $\gamma\delta$ T cell subsets
33 making either IFN- γ or IL-17 have intrinsically distinct metabolic requirements.
34 Whereas IFN- γ^+ $\gamma\delta$ T cells were almost exclusively dependent on glycolysis,
35 IL-17 $^+$ $\gamma\delta$ T cells strongly engaged oxidative metabolism, with increased
36 mitochondrial mass and activity. These distinct metabolic signatures were
37 surprisingly imprinted early during thymic development, and were stably
38 maintained in the periphery and within tumours. Moreover, pro-tumoural IL-
39 17 $^+$ $\gamma\delta$ T cells selectively showed high lipid uptake and intracellular lipid
40 storage, and were expanded in obesity, and in tumours of obese mice.
41 Conversely, glucose supplementation enhanced the anti-tumour functions of
42 IFN- γ^+ $\gamma\delta$ T cells and reduced tumour growth upon adoptive transfer. These
43 findings have important implications for the differentiation of effector $\gamma\delta$ T cells
44 and their manipulation in cancer immunotherapy.

45

46 **Introduction**

47 T cells engage specific metabolic pathways to support their differentiation,
48 proliferation and function^{1,2}. Whereas naive $\alpha\beta$ T cells oxidize glucose-derived
49 pyruvate *via* oxidative phosphorylation (OXPHOS) or fatty acid oxidation
50 (FAO) to generate ATP, most effector $\alpha\beta$ T cells engage in aerobic glycolysis
51 (“Warburg effect”), i.e. the conversion of glucose to lactate, to strengthen cell
52 growth and proliferation³. On the other hand, while aerobic glycolysis is
53 required for optimal $\alpha\beta$ T cell effector function^{4,5}, tumour cells heavily
54 consume glucose in the tumour microenvironment (TME), which has a
55 dramatic impact on cytokine production by T cells and hampers tumour
56 immunity^{5,6}. There is therefore great interest in understanding how
57 metabolism-based interventions could inhibit tumour metabolism while
58 promoting effective anti-tumour immunity for improved immunotherapeutic
59 outcomes⁷.

60 $\gamma\delta$ T cells represent a promising immune population for next-generation
61 cancer immunotherapies^{8,9}. Since they are not MHC-restricted nor dependent
62 on neoantigen recognition, $\gamma\delta$ T cells constitute a complementary layer of anti-
63 tumour immunity to their $\alpha\beta$ T cell counterparts¹⁰. In fact, many properties of
64 $\gamma\delta$ T cells, including sensing of “stress-inducible” changes and very rapid
65 effector responses, align best with innate immunity, or “lymphoid stress-
66 surveillance”¹¹, although in some instances they display adaptive-like
67 behaviour and profound shaping of T cell receptor (TCR) repertoires^{12,13}.

68 The effector functions of murine $\gamma\delta$ T cells are dominated by the production of
69 two key cytokines, interleukin 17A (IL-17) and interferon- γ (IFN- γ). Beyond
70 contributions to immune responses against pathogens, the provision of these
71 two cytokines by $\gamma\delta$ T cells is important in many (patho)physiological contexts,
72 such as maintenance of tissue homeostasis^{14,15}, autoimmunity¹⁶ and cancer⁸.
73 IL-17 and IFN- γ are mostly produced by distinct $\gamma\delta$ T cell subsets that, unlike
74 their CD4⁺ T cell counterparts, typically acquire their effector functions during
75 thymic development^{17,18}. Thus, we and others have shown that thymic $\gamma\delta$ T
76 cell progenitors, driven by signals including those stemming from the TCR,

77 split into a CD27⁺ (and CD45RB⁺) branch that makes IFN- γ but not IL-17; and
78 a CD27⁻ (and CD44^{hi}) pathway that selectively expresses IL-17¹⁷⁻²¹.

79 The IFN- γ /IL-17 dichotomy between effector $\gamma\delta$ T cell subsets is particularly
80 relevant in cancer, since IFN- γ -producing $\gamma\delta$ T cells ($\gamma\delta^{\text{IFN}}$) are associated with
81 tumour surveillance and regression, whereas IL-17-secreting $\gamma\delta$ T cells ($\gamma\delta^{17}$)
82 promote primary tumour growth and metastasis, both in mice and in
83 humans^{8,22}. However, the molecular cues that regulate the balance between
84 such antagonistic $\gamma\delta$ T cell subsets in the TME remain poorly characterized.
85 Given the strong impact of metabolic resources on anti-tumour $\alpha\beta$ T cell
86 responses, here we have investigated the metabolic profiles of $\gamma\delta$ T cell
87 subsets and how they might impact on their activities in the TME. We found
88 that $\gamma\delta^{\text{IFN}}$ T cells are almost exclusively glycolytic, whereas $\gamma\delta^{17}$ T cells are
89 strongly dependent on mitochondrial and lipid oxidative metabolism. This
90 metabolic dichotomy is established in the thymus during $\gamma\delta$ T cell
91 development, and maintained in peripheral lymphoid organs and within
92 tumours in various experimental models of cancer. We further show that the
93 provision of glucose or lipids has major impact on the relative expansion and
94 function of the two $\gamma\delta$ T cell subsets, and this can be used to enhance anti-
95 tumour $\gamma\delta$ T cell responses.

96

97

98

99 Results

100 Intra-tumoural $\gamma\delta$ T cell subsets display distinct metabolic profiles

101 The analysis of metabolic profiles of tumour-infiltrating $\gamma\delta$ T cells ($\gamma\delta$ TILs)
102 presented a major challenge: the low numbers that can be retrieved from
103 tumour lesions in mice are largely incompatible with techniques such as
104 Seahorse metabolic flux analysis. To overcome this difficulty, we used a
105 newly developed protocol, SCENITH™ (*Single Cell mEtabolism by profiling*
106 *Translation inHibition*), which is a flow cytometry-based method for profiling
107 energy metabolism with single cell resolution²³. This method is based on
108 metabolism-dependent translation rates and puromycin's incorporation into
109 nascent proteins (**Supplementary Fig. 1a**). The use of specific inhibitors
110 allows the estimation of glucose dependence, mitochondrial dependence,
111 glycolytic capacity and fatty acid and amino acid oxidation (FaaO) capacity
112 (**Supplementary Fig. 1b**). We employed SCENITH™ to analyze the
113 metabolic profiles of $\gamma\delta$ TILs isolated from tumour lesions in well-established
114 mouse models of breast (E0771) and colon (MC38) cancer (**Fig. 1a**). In both
115 cancer models, and at both later (**Fig. 1b,c**) and earlier time points (**Fig.**
116 **1d,e**), we observed that $\gamma\delta^{\text{IFN}}$ cells had substantially higher glycolytic capacity,
117 whereas $\gamma\delta^{17}$ cells were strongly dependent on mitochondrial activity (**Fig. 1b-**
118 **e**). These data, obtained in cancer models, prompted us to investigate the
119 metabolic phenotypes of $\gamma\delta$ T cell subsets in multiple tissues at steady state.

120

121 Peripheral $\gamma\delta$ T cell subsets show different mitochondrial and metabolic 122 phenotypes

123 To explore the metabolic differences between $\gamma\delta$ T cell subsets in peripheral
124 tissues, we analysed mitochondria, given their central role in cellular
125 metabolism. To distinguish between $\gamma\delta^{\text{IFN}}$ and $\gamma\delta^{17}$ cells we used CD27
126 expression¹⁸⁻²¹. CD27⁻ $\gamma\delta$ ($\gamma\delta^{17}$) cells displayed increased mitotracker and
127 tetramethylrhodamine methyl ester (TMRM) staining in peripheral lymph
128 nodes (LNs) compared to CD27⁺ $\gamma\delta$ ($\gamma\delta^{\text{IFN}}$) cells, indicating higher
129 mitochondrial mass (normalised to cell size) and mitochondrial membrane

130 potential ($\Delta\Psi_m$), respectively (**Fig. 2a,b**). These differences were retained
131 upon activation and expansion *in vitro* over 9-days (**Supplementary Fig. 2**).
132 Importantly, the distinct mitochondrial phenotypes were also validated with
133 another mitochondrial membrane potential dye, tetramethylrhodamine ethyl
134 ester (TMRE), and were features of $\gamma\delta^{17}$ and $\gamma\delta^{\text{IFN}}$ cells *ex vivo* from multiple
135 locations (**Fig. 2c**). In agreement with mitochondrial enrichment in $\gamma\delta^{17}$ cells,
136 seahorse metabolic flux analysis of peripheral $\gamma\delta$ T cells showed higher levels
137 of basal OXPHOS in $\gamma\delta^{17}$ cells, and conversely, increased basal levels of
138 glycolysis in $\gamma\delta^{\text{IFN}}$ cells (**Fig. 2d-f**). These data were validated in independent
139 experiments using SCENITHTM on splenic and LN $\gamma\delta$ T cell subsets (**Fig. 2g**).

140 To assess if this metabolic dichotomy had an underlying transcriptional basis,
141 we measured the mRNA levels of key mitochondrial and glycolysis-associated
142 genes in purified peripheral $\gamma\delta^{17}$ and $\gamma\delta^{\text{IFN}}$ cells. We found systematic biases in
143 gene expression that matched the differential metabolic programmes (**Fig.**
144 **2h,i**). Of particular note is the clear-cut segregation of two master
145 transcriptional regulators: *Nrf1*, which orchestrates mitochondrial DNA
146 transcription^{24,25}, found to be enriched in $\gamma\delta^{17}$ cells (**Fig. 2h**); and *Myc*, which
147 controls glycolysis^{26,27}, that was highly overexpressed in $\gamma\delta^{\text{IFN}}$ cells (**Fig. 2i**).
148 *Myc* expression was further validated using a *Myc*-GFP reporter mouse (**Fig.**
149 **2j**). These data collectively demonstrated that $\gamma\delta$ T cell subsets possess
150 distinct mitochondrial and metabolic features in peripheral organs at steady
151 state.

152

153 **$\gamma\delta$ T cell subsets are metabolically programmed in the thymus**

154 We next aimed to understand when, during their differentiation, the metabolic
155 differences between the two effector $\gamma\delta$ T cell subsets were established. Since
156 most $\gamma\delta$ T cells are functionally pre-programmed in the thymus, we examined
157 $\gamma\delta$ thymocyte sub-populations. Our recent studies have identified sequential
158 stages of thymic $\gamma\delta$ T cell progenitor development marked by CD24, CD44
159 and CD45RB¹⁹. Early CD24⁺ ($\gamma\delta^{24+}$) precursors downregulate CD24 to
160 become a CD24⁻CD44⁻CD45RB⁻ ($\gamma\delta^{\text{TN}}$) population that can generate cells

161 committed to either IL-17 or IFN- γ expression, which display respectively
162 CD44^{hi}CD45RB⁻ ($\gamma\delta^{17}$) and CD44⁺CD45RB⁺ ($\gamma\delta^{\text{IFN}}$) phenotypes
163 (**Supplementary Fig 3**). By using the SCENITHTM method, we found that, in
164 both the adult (**Fig. 3a**) and newborn (**Fig. 3b**) thymus, these subsets showed
165 the same metabolic dichotomy as in the periphery (**Fig. 2g**), although this was
166 less distinct in $\gamma\delta$ thymocytes, likely due to the dynamic subset segregation
167 process¹⁹.

168 To investigate any potential switching of metabolic programming during $\gamma\delta$
169 thymocyte development, we first compared early thymic $\gamma\delta$ progenitors with
170 more mature subpopulations already committed to IL-17 or IFN- γ production.
171 We found that $\gamma\delta^{24+}$ and $\gamma\delta^{\text{TN}}$ progenitors stained highly for TMRE, that was
172 lost when $\Delta\Psi\text{m}$ was dissipated by the ionophore carbonyl cyanide-4-
173 (trifluoromethoxy) phenylhydrazone (FCCP) (**Fig. 3c,d**). Interestingly,
174 whereas $\gamma\delta^{17}$ cells retained a high level of TMRE staining, $\gamma\delta^{\text{IFN}}$ cells showed a
175 marked reduction in $\Delta\Psi\text{m}$ suggesting a metabolic switch away from OxPhos
176 (**Fig. 3d**). Moreover, imagestream analysis of $\gamma\delta^{17}$ cells stained with either
177 mitotracker or TMRE revealed large and active mitochondria, in contrast with
178 $\gamma\delta^{\text{IFN}}$ cells that displayed negligible staining for either dye (**Fig. 3e**), in line with
179 our previous observations in peripheral subsets (**Fig. 2a-c**). Furthermore,
180 Seahorse extracellular flux analysis showed that $\gamma\delta^{17}$ thymocytes have both
181 higher maximal respiration potential and spare respiratory capacity than their
182 $\gamma\delta^{\text{IFN}}$ counterparts (**Fig. 3f,g**). Thus, $\gamma\delta$ T cell subsets acquire distinct
183 mitochondrial features during their acquisition of effector function in the
184 thymus.

185 The adoption of divergent metabolic programs by thymic $\gamma\delta$ T cell subsets
186 suggested they could thrive under distinct metabolic environments. To begin
187 to address this, we placed WT E15 thymic lobes in 7-day foetal thymic organ
188 cultures (E15 + 7d FTOC) with media containing either low or high amounts of
189 glucose (**Fig. 3h**). $\gamma\delta^{17}$ cells were readily detected in lower glucose conditions
190 but failed to develop to normal numbers when glucose concentrations were
191 raised. By contrast, $\gamma\delta^{\text{IFN}}$ cells were relatively enriched in high glucose
192 conditions as demonstrated by a significant decrease in the $\gamma\delta^{17}/\gamma\delta^{\text{IFN}}$ cell

193 ratio (**Fig. 3h**). We next established E15 + 7d FTOC in the presence of the
194 glycolysis inhibitor 2-deoxy-D-glucose (2-DG), and found increased numbers
195 of $\gamma\delta^{17}$ cells and increased $\gamma\delta^{17}/\gamma\delta^{\text{IFN}}$ cell ratios (**Fig. 3i**). A similar result was
196 observed in E15 + 7d FTOC when cultured with Fasentin that blocks glucose
197 uptake (**Supplementary Fig. 4**). By contrast, running E15 + 7d FTOC in the
198 presence of metformin, which reduces the efficiency of OxPhos by inhibiting
199 complex I of the electron transport chain, impaired $\gamma\delta^{17}$ cell generation and
200 decreased the $\gamma\delta^{17}/\gamma\delta^{\text{IFN}}$ cell ratio (**Fig. 3j**). Collectively, these results suggest
201 that the mitochondrial characteristics adopted by $\gamma\delta^{17}$ and $\gamma\delta^{\text{IFN}}$ cells during
202 thymic development directly impact their ability to thrive in distinct metabolic
203 environments.

204

205 **Distinct mitochondrial activities underlie effector fate of thymic $\gamma\delta$ T cell** 206 **precursors**

207 We next aimed to investigate the association of distinct metabolic
208 programmes with the developmental divergence of $\gamma\delta^{17}$ and $\gamma\delta^{\text{IFN}}$ cells in the
209 thymus. Although the $\gamma\delta^{\text{TN}}$ population, i.e. the progenitor $\gamma\delta$ cell subset that
210 immediately precedes the surface upregulation of either CD44 or CD45RB
211 (marking commitment to the IL-17 or IFN- γ pathways, respectively¹⁹) was
212 predominantly TMRE^{hi}, we observed a fraction of cells with reduced TMRE
213 staining that we reasoned might be transitioning to the TMRE^{lo} state shown by
214 $\gamma\delta^{\text{IFN}}$ cells (**Fig. 3c**). We further hypothesized that the metabolic status of $\gamma\delta^{\text{TN}}$
215 progenitors may predict their developmental fate. To test this, we sorted
216 TMRE^{hi} and TMRE^{lo} cells from the $\gamma\delta^{\text{TN}}$ subset obtained from E15 + 7d FTOC,
217 and cultured them for 5-days on OP9-DL1 cells that are known to support
218 appropriate development of thymocytes²⁸. As predicted, virtually all cells from
219 the TMRE^{lo} cultures upregulated CD45RB and entered the IFN γ -pathway
220 (**Fig. 4a**); however, we were surprised that almost all cells from the TMRE^{hi}
221 cultures entered the CD44^{hi} IL-17-pathway (**Fig. 4a**). This strongly suggests
222 that $\gamma\delta^{\text{TN}}$ cells have already committed to an effector fate, and that this
223 commitment associates with distinct mitochondrial activities.

224 To pursue this hypothesis further, we tested $\gamma\delta^{24+}$ progenitors that immediately
225 precede the $\gamma\delta^{\text{TN}}$ subset; again, we observed a remarkable segregation of
226 effector fate, with the majority of $\text{TMRE}^{\text{lo}} \gamma\delta^{24+}$ cells entering the $\text{IFN}\gamma$ -
227 pathway, and the majority of $\text{TMRE}^{\text{hi}} \gamma\delta^{24+}$ cells entering the IL-17-pathway
228 (**Fig. 4b**). The observation that so few $\text{TMRE}^{\text{hi}} \gamma\delta^{24+}$ cells adopt an $\text{IFN}\gamma$ -
229 secreting fate again suggests that most $\gamma\delta^{24+}$ progenitors have already
230 committed to subsequent effector function. Moreover, we found that
231 differences in TMRE levels correlated with the known^{18,20,21} effector biases of
232 $V\gamma 1^+$ ($\gamma\delta^{\text{IFN}}$ -biased) and $V\gamma 4^+$ ($\gamma\delta^{17}$ -biased) progenitors (**Fig. 4c**); and validated
233 the early TMRE-based segregation of effector fates using only $V\gamma 4^+$
234 progenitors (**Supplementary Fig 5**). Furthermore, among $\gamma\delta^{24+}$ thymocytes
235 along the $\gamma\delta^{\text{IFN}}$ pathway, we observed a progressive downregulation of TMRE
236 levels from $\gamma\delta^{\text{TN}}$ to $\text{CD44}^{\text{lo}}\text{CD45RB}^+$ cells and finally $\gamma\delta^{\text{IFN}}$ cells (**Fig. 4d**).

237 Given that we and others^{20,21} have previously shown a key role for TCR
238 signalling in $\gamma\delta^{\text{IFN}}$ thymocyte differentiation, we next asked if downregulation of
239 TMRE levels associated with hallmarks of TCR signalling. Indeed, we found
240 that low TMRE associated with high expression of CD73 (**Fig. 4e**), one of the
241 best established markers of TCR signalling in $\gamma\delta$ T cell development^{20,28,29}.
242 Moreover, in E15 thymic lobes, TMRE staining was reduced along with CD25
243 downregulation, which is another hallmark of (developmentally early) $\text{TCR}\gamma\delta$
244 signalling^{18,20,21} (**Fig. 4f**). Furthermore, at this E15 stage, the cells with the
245 lowest TMRE staining were $V\gamma 5^+$ progenitors (**Fig. 4f**) that are known to
246 engage a Skint1-associated TCR-ligand in the thymus and to uniformly
247 commit to the $\text{IFN}\gamma$ -pathway³⁰.

248 These lines of evidence suggested that $\gamma\delta$ progenitors receiving agonist
249 $\text{TCR}\gamma\delta$ signals shift away from OxPhos as indicated by their reduced $\Delta\Psi\text{m}$.
250 To strengthen this point, we manipulated TCR signals using agonist GL3
251 mAb, which, as expected^{18,19}, promoted $\gamma\delta^{\text{IFN}}$ cell development while inhibiting
252 the $\gamma\delta^{17}$ pathway in E17 + 6d FTOC (**Fig. 4g**). Upon specifically sorting
253 $\text{TMRE}^{\text{hi}} \gamma\delta^{24+}$ cells from E17 thymi and stimulating them with GL3 for 5h, we
254 found a subpopulation that downregulated CD24 together with TMRE levels, in
255 a mAb dose-dependent dose manner (**Fig. 4h**). These results strongly

256 suggest that TCR signalling leads to $\Delta\Psi_m$ downregulation as $\gamma\delta$ thymocytes
257 differentiate into IFN- γ producers.

258 To gain further molecular resolution, we performed single-cell
259 RNAsequencing on TMRE^{lo} and TMRE^{hi} $\gamma\delta^{24+}$ cells from E15 + 2d FTOC (**Fig.**
260 **4i-l**). Using UMAP, TMRE^{lo} cells clustered clearly away from TMRE^{hi} $\gamma\delta^{24+}$
261 cells (**Fig. 4j**), and the former were enriched in genes involved in the
262 regulation of antigen receptor signalling (**Fig. 4k**). In support of the metabolic
263 phenotypes observed *ex vivo*, genes associated with OxPhos were enriched
264 specifically in TMRE^{hi} $\gamma\delta^{24+}$ cells while genes involved in glucose metabolism
265 were unregulated in TMRE^{lo} $\gamma\delta^{24+}$ cells (**Fig. 4l**).

266 These data collectively demonstrate that metabolic status of thymic $\gamma\delta$
267 progenitors marks their developmental fate from a very early stage.
268 Progenitors entering the IL-17 pathway display sustained high mitochondrial
269 activity, whereas those in the IFN- γ pathway undergo a TCR-induced
270 metabolic shift towards aerobic glycolysis. We next questioned how these
271 intrinsic metabolic differences impacted the physiology of effector $\gamma\delta$ T cell
272 subsets.

273

274 **Enrichment of lipid storage and lipid metabolism in $\gamma\delta^{17}$ cells**

275 Having shown that, in stark contrast with $\gamma\delta^{\text{IFN}}$ cells, $\gamma\delta^{17}$ cell generation was
276 reduced under high glucose concentrations (**Fig. 3h**), and enhanced upon
277 inhibition of glycolysis (**Fig. 3i**) or glucose uptake (**Supplementary Fig. 4**), we
278 questioned whether other metabolic resources may be important for $\gamma\delta^{17}$ cell
279 physiology. To address this question we took advantage of reporter mice
280 (*Zbtb16*^{GFP}) for another marker that segregates $\gamma\delta^{17}$ and $\gamma\delta^{\text{IFN}}$ cells, the
281 transcription factor PLZF (encoded by *Zbtb16*)^{21,14,31}. We performed RNA-
282 sequencing of lymphoid and tissue-resident $\gamma\delta$ T cells sorted into PLZF⁺ ($\gamma\delta^{17}$)
283 and PLZF⁻ ($\gamma\delta^{\text{IFN}}$) cells (**Fig. 5a**). As expected, $\gamma\delta^{17}$ cells across tissues
284 expressed *Il17a*, whereas *Il17f* was also expressed in tissue-resident $\gamma\delta^{17}$
285 cells (**Fig. 5b**). Different metabolic pathways were associated with lymphoid
286 versus tissue resident $\gamma\delta$ T cells however, the genes common to $\gamma\delta^{17}$ cells

287 across all tissues were related to lipid and mitochondrial metabolism,
288 including glutamate transporter (*Slc1a1*), glucose/fatty acid metabolism
289 (*Pdk4*), mitochondrial protein transport (*Ablim3*) and lipid metabolism (*Fabp1*,
290 *Abdh5*, *Atp10a*). These data highlight genes associated with lipid metabolism
291 as a common feature of $\gamma\delta^{17}$ T cells across tissues. Consistent with this, LN
292 $\gamma\delta^{17}$ cells had a higher neutral lipid content (as assessed by LipidTOX
293 staining) than $\gamma\delta^{\text{IFN}}$ cells (**Fig. 5 c,d**). This differential lipid content was further
294 increased upon activation with IL-1 β +IL-23 (**Supplementary Fig. 6a**),
295 associated with expression of IL-17A, IL-17F and ROR γ t (**Supplementary**
296 **Fig. 6b**), and was observed across $\gamma\delta$ T cells from multiple tissues, with the
297 notable exception of the skin (**Fig. 5e**), where $\gamma\delta$ T cells have been shown to
298 display specific mechanisms of tissue adaptation³². In particular, V γ 6⁺ $\gamma\delta$ T
299 cells in the dermis are transcriptionally distinct from those in pLNs and display
300 a highly activated but less proliferative phenotype. This tissue adaptation may
301 alter the metabolic requirements of skin-resident $\gamma\delta$ T cells. In addition, $\gamma\delta$ T
302 cells may adapt to utilize specific metabolites present within the skin³³.

303 Imaging analysis revealed that the increased LipidTOX staining was due to
304 the accumulation of intracellular lipid droplets in $\gamma\delta^{17}$ cells (**Fig. 5f,g**). Lipid
305 droplets store neutral lipids including triglycerides (TAGs) and cholesterol
306 esters³⁴. We found that the two $\gamma\delta$ subsets had equivalent TAG content (**Fig.**
307 **5h**) but free cholesterol, as determined by Filipin III staining, was higher in
308 $\gamma\delta^{17}$ cells (**Fig. 5i**). We next questioned if $\gamma\delta^{17}$ engaged in lipid uptake which
309 could account for lipid storage. Using labelled palmitate (Bodipy-FL-C₁₆), we
310 found that $\gamma\delta^{17}$ cells selectively took up lipids (**Fig. 5j**), which was further
311 enhanced following activation (**Supplementary Fig. 6c**). Analysis of $\gamma\delta$ T cell
312 cytokine production confirmed that the ability to take up palmitate was specific
313 to IL-17 producers (**Fig. 5l,m**). Of note, V γ 4⁺ and V γ 6⁺ (V γ 1⁻V γ 4⁺) $\gamma\delta$ T cells
314 showed a higher palmitate uptake than V γ 1⁺ cells (**Fig. 5n**); While V γ 6⁺ $\gamma\delta$ T
315 cells primarily produce IL-17, V γ 4⁺, can produce either IFN- γ or IL-17^{18,19}.
316 However, palmitate uptake was specific to V γ 4⁺ cells that produced IL-17 (**Fig.**
317 **5o**). Furthermore, $\gamma\delta^{17}$ cells also displayed higher uptake of fluorescently
318 labelled cholesterol ester (Bodipy CholEsteryl FL-C₁₂) (**Fig. 5k**), indicating

319 their ability to take up multiple types of lipids including fatty acids and
320 cholesterol.

321 These data demonstrate that $\gamma\delta^{17}$ cells have an exquisite capacity to take up
322 and accumulate intracellular lipids, and display transcriptional signatures of
323 enhanced lipid metabolism compared to $\gamma\delta^{\text{IFN}}$ cells.

324

325 **High fat diet promotes $\gamma\delta^{17}$ cell expansion and their accumulation in** 326 **tumours**

327 We next tested the effect of a lipid-rich, high fat diet (HFD), on $\gamma\delta$ T cell
328 subsets *in vivo*. Unlike standard fat diet (SFD) fed mice, which alternate
329 between using lipids or carbohydrates for fuel during light/dark cycles
330 respectively, feeding mice a HFD reduced their respiratory exchange ratio
331 (RER), illustrating a systemic metabolic switch to constantly burning lipids as
332 the main fuel source. (**Fig. 6a**). We found that both the percentage and
333 absolute number of LN $\gamma\delta$ T cells were increased during HFD (**Fig. 6b**), which
334 was due to a specific increase in $\gamma\delta^{17}$ (but not $\gamma\delta^{\text{IFN}}$) cells (**Fig. 6c,d**).

335 Tumours are another site reported to be lipid-rich. To explore the effect of the
336 lipid-rich tumour environment on $\gamma\delta^{17}$ cells, we employed the B16F10
337 melanoma model. In SFD mice, we found an enrichment of $\gamma\delta^{17}$ cells within
338 the tumour compared to draining LN (dLN) or spleen (**Fig. 6e**). These $\gamma\delta^{17}$
339 cells were also enriched compared to $\gamma\delta^{\text{IFN}}$ (**Fig. 6f**). Given $\gamma\delta^{17}$ were enriched
340 in obese mice and in the tumour, we next asked if obesity combined with the
341 tumour model would further enhance $\gamma\delta^{17}$ cells. Mice fed HFD exhibited
342 enhanced tumour growth (**Fig. 6g**), and further increased percentages and
343 numbers of tumour-infiltrating $\gamma\delta^{17}$ cells compared to the SFD group (**Fig. 6 h-**
344 **j**). These data demonstrate that a lipid-rich environment selectively
345 accumulates $\gamma\delta^{17}$ but not $\gamma\delta^{\text{IFN}}$ cells in the tumour.

346 Given the preferential uptake of cholesterol by $\gamma\delta^{17}$ cells (**Fig. 5i**), we next
347 investigated its effect on $\gamma\delta^{17}$ cell proliferation and function. We incubated
348 purified $\gamma\delta^{27-}$ ($\gamma\delta^{17}$) cells for 5h with cholesterol-loaded cyclodextrin (CLC),
349 which we found to promote $\gamma\delta^{27-}$ cell proliferation when compared to control

350 culture conditions (**Fig. 6k**). To determine its impact on tumor growth *in vivo*,
351 we injected CLC pre-treated (or control) $\gamma\delta^{17}$ cells twice (within two days) into
352 s.c. E0771 tumours (as established in **Fig. 1b**), which allow local T cell
353 delivery. Strikingly, $\gamma\delta^{17}$ cells pre-treated with CLC substantially enhanced
354 tumour growth (**Fig. 6l-n**).

355 Conversely, we also tested the effect of reducing lipids *in vivo*, by injected
356 orlistat, which inhibits lipases and thus prevents uptake of dietary fat, into
357 B16F10 tumour-bearing mice. Mice injected with orlistat exhibited reduced
358 body weight and tumour growth compared to vehicle-treated mice
359 (**Supplementary Fig. 7a,b**). Importantly, these mice showed decreased
360 numbers of tumour-infiltrating $\gamma\delta^{17}$ cells, which had lower neutral lipid content
361 (**Supplementary Fig. 7c,d**).

362 Together, these data show that lipid-rich environments promote the selective
363 expansion of $\gamma\delta^{17}$ cells that support tumour growth.

364

365 **Glucose supplementation enhances anti-tumour functions of $\gamma\delta^{\text{IFN}}$ cells**

366 We next aimed to use the knowledge gathered in this study to boost anti-
367 tumour $\gamma\delta$ T cell responses, which are known to rely on $\gamma\delta^{\text{IFN}}$ cells^{8,22}. Given
368 our data showing that glucose promotes the development of $\gamma\delta^{\text{IFN}}$ over $\gamma\delta^{17}$
369 cells in the thymus (**Fig. 3h,i**), and the higher glycolytic capacity of $\gamma\delta^{\text{IFN}}$ cells
370 in peripheral organs (**Fig. 2g**) and also within tumours (**Fig. 1b-e**), we
371 hypothesized that glucose supplementation would enhance $\gamma\delta^{\text{IFN}}$ cell
372 functions. Further supporting this hypothesis, we found that intra-tumoural
373 $\gamma\delta^{\text{IFN}}$ cells preferentially took up 2-NDBG when compared to $\gamma\delta^{17}$ TILs (**Fig.**
374 **7a**).

375 We first tested the impact of glucose on $\gamma\delta^{17}$ and $\gamma\delta^{\text{IFN}}$ cell functions *in vitro*.
376 We cultured purified $\gamma\delta^{27-}$ ($\gamma\delta^{17}$) or $\gamma\delta^{27+}$ ($\gamma\delta^{\text{IFN}}$) cells in standard culture
377 conditions containing low dose glucose (5mM) or in high glucose (50mM). We
378 found high glucose to be detrimental to $\gamma\delta^{17}$ cells (**Supplementary Fig. 8**), in
379 stark contrast to $\gamma\delta^{\text{IFN}}$ cells. Indeed, supplementation with high glucose
380 augmented (whereas provision of 2-DG reduced) the percentage and

381 numbers of $\gamma\delta^{\text{IFN}}$ cells (**Fig. 7b**), with parallel effects on their proliferation (**Fig.**
382 **7c**) and on the levels of expression of both IFN- γ (**Fig. 7d**) and its master
383 transcriptional regulator²¹, T-bet (**Fig. 7e**).

384 To specifically address the importance of aerobic glycolysis for $\gamma\delta^{\text{IFN}}$ cells, we
385 cultured $\gamma\delta^{\text{IFN}}$ cells with galactose (compared to glucose), since cells grown in
386 galactose enter the pentose phosphate pathway instead of using aerobic
387 glycolysis^{35,36}. We observed a reduction in the percentage and absolute
388 numbers of $\gamma\delta^{\text{IFN}}$ cells (**Fig. 7f**), as well as in their IFN- γ (**Fig. 7g**) and T-bet
389 (**Fig. 7h**) expression levels, thus establishing that aerobic glycolysis is
390 required for optimal IFN- γ production by $\gamma\delta^{\text{IFN}}$ cells.

391 Next we asked if the cytotoxic function of $\gamma\delta^{\text{IFN}}$ cells was also enhanced by
392 glucose supplementation. For this, we co-cultured $\gamma\delta^{\text{IFN}}$ cells that were
393 previously supplemented (or not) with high dose of glucose with E0771 breast
394 cancer cells at different effector:target (E:T) ratios. “Glucose-enhanced” $\gamma\delta^{\text{IFN}}$
395 cells displayed substantially higher cytotoxic potency against the cancer cells,
396 compared to the respective controls at each E:T ratio (**Fig. 7i**).

397 As $\gamma\delta$ T cells are actively being pursued in the clinic as an adoptive cell
398 therapy for cancer⁸, we tested whether we could use glucose supplementation
399 to enhance the anti-tumour functions of $\gamma\delta^{\text{IFN}}$ cells *in vivo*, in an adoptive cell
400 transfer setting. Purified $\gamma\delta^{\text{IFN}}$ cells were cultured in the presence or absence
401 of high dose glucose for 5h, washed, and injected twice (within two days) into
402 the tumour site. While control $\gamma\delta^{\text{IFN}}$ cells produced a small yet significant
403 reduction in tumour size, glucose substantially augmented the anti-tumour
404 effects of $\gamma\delta^{\text{IFN}}$ cells, essentially inhibiting tumour growth (from the time of
405 injection) within the time window analysed (**Fig. 7j,k**). These data reveal a
406 new, metabolism-based, means to enhance the anti-tumour functions of $\gamma\delta$ T
407 cells that could be explored for adoptive cell immunotherapy of cancer.

408 Discussion

409 Metabolism dysregulation is viewed as an immune evasion strategy in cancer.
410 To overcome it, and thus enable anti-tumour immune responses, it is critical
411 to understand immune cell metabolism and its interplay with tumour cells in
412 the TME. Although our knowledge on $\alpha\beta$ T cell metabolism has increased
413 significantly^{1,3,37}, little is known about $\gamma\delta$ T cells. Here, we identified a
414 metabolic dichotomy between the main effector $\gamma\delta$ T cell subsets that play
415 opposing roles in cancer immunity^{8,22}. Whereas anti-tumoural $\gamma\delta^{\text{IFN}}$ cells are
416 almost exclusively glycolytic, pro-tumoural $\gamma\delta^{17}$ cells require mitochondrial
417 metabolism; and their activities within tumours can be promoted by glucose or
418 lipid metabolism, respectively.

419 Unexpectedly, the metabolic dichotomy of $\gamma\delta$ T cell subsets is established
420 early during thymic development, which contrasts with the peripheral
421 metabolic (re)programming of effector $\alpha\beta$ T cells. Naïve $\alpha\beta$ T cells require
422 activation to undergo rewiring of cellular metabolism, namely transition from
423 OxPhos to aerobic glycolysis, through which glucose is fermented into lactate
424 rather than oxidized in mitochondria³. Furthermore, depending on metabolic
425 cues in the tissue or during immune challenge, naïve T cells are pushed
426 toward Th1, Th2, Th17 or Treg fates, dependent on intrinsic metabolic
427 pathways engaged outside the thymus. By contrast, we show that an
428 equivalent metabolic shift occurs in early thymic $\gamma\delta$ progenitors as they
429 commit to the IFN- γ pathway, seemingly as a result of strong TCR $\gamma\delta$
430 signalling. Indeed, analysis of various hallmarks of TCR signalling suggest
431 that $\gamma\delta$ progenitors receiving agonist TCR $\gamma\delta$ signals shifted away from OxPhos
432 as indicated by their reduced $\Delta\Psi\text{m}$. Moreover, upon TCR (GL3 mAb)
433 stimulation, a small population of $\gamma\delta$ progenitors downregulated CD24
434 together with $\Delta\Psi\text{m}$ (TMRE), thus associating strong TCR $\gamma\delta$ signalling in the
435 $\gamma\delta^{\text{IFN}}$ developmental pathway with metabolic reprogramming. This draws a
436 parallel with $\alpha\beta$ T cell activation, during which early TCR signalling is required
437 for induction of aerobic glycolysis³⁸. This acts as a switch for *Myc* mRNA (and
438 protein) expression, such that strength of TCR stimulus determines the
439 frequency of T cells that transcribe *Myc* mRNA³⁶. The common denominator

440 of the metabolic switches in effector $\gamma\delta$ and $\alpha\beta$ T cells may thus be
441 upregulation of Myc, which is required for transcription of genes encoding
442 glycolytic enzymes^{26,27}. Indeed, our data show a striking enrichment of Myc
443 (mRNA and protein) in $\gamma\delta^{\text{IFN}}$ cells compared to $\gamma\delta^{17}$ cells. On the other hand,
444 the sustained dependence of $\gamma\delta^{17}$ cells on mitochondrial OxPhos is in line with
445 that recently reported for their functional equivalents in the $\alpha\beta$ T cell
446 compartment, Th17 cells³⁹. Of note, IL-17-producing type 3 innate lymphoid
447 cells (ILC3) were recently shown to require both glycolysis and mitochondrial-
448 derived ROS for activation⁴⁰, but a direct comparison with type 1 ILCs is still
449 missing.

450 The concept of TCR signalling playing a key role in the metabolic
451 programming of $\gamma\delta$ T cell subsets builds upon, but provides a novel
452 perspective to, previous models of their thymic development. Thus, the
453 unequivocal dependence on strong TCR signals for $\gamma\delta^{\text{IFN}}$ cell
454 differentiation^{20,30} may be linked to a required metabolic shift to aerobic
455 glycolysis. Moreover, the detrimental impact of agonist TCR signals on $\gamma\delta^{17}$
456 cell development may be due to metabolic conflict with their OxPhos
457 requirements, documented by our FTOC experiments using specific inhibitors.
458 Importantly, these distinct metabolic phenotypes are maintained in peripheral
459 $\gamma\delta$ T cell subsets, which is consistent with and expands our previous
460 epigenetic and transcriptional analyses^{41,42}.

461 We were particularly interested to investigate the metabolic properties of
462 peripheral $\gamma\delta$ T cell subsets once they infiltrated tumour lesions, for which we
463 employed three experimental models of cancer (melanoma, breast and
464 colon). Critically, we found that the dichotomy between $\gamma\delta^{17}$ and $\gamma\delta^{\text{IFN}}$ subsets
465 was preserved in the TME, which enabled metabolic interventions that may
466 have therapeutic potential. In fact, while $\gamma\delta$ T cell infiltration is largely
467 perceived to associate with favourable prognosis in cancer patients⁴³, recent
468 clinical data have suggested that, in agreement with mouse experimental
469 systems²², human $\gamma\delta^{17}$ *versus* $\gamma\delta^{\text{IFN}}$ cell subsets have antagonistic prognostic
470 values⁸. Thus, improvement in the therapeutic performance of $\gamma\delta$ T cells in the

471 clinic⁴⁴ is likely to require a better understanding of the factors that control the
472 balance between $\gamma\delta^{17}$ and $\gamma\delta^{\text{IFN}}$ cell subsets in the TME.

473

474 Here, we also identified lipids as key $\gamma\delta^{17}$ -promoting factors, which is
475 particularly relevant because tumours are known to be lipid-rich
476 microenvironments^{4,5,45,46}. Palmitate and cholesterol ester uptake were higher
477 in $\gamma\delta^{17}$ than $\gamma\delta^{\text{IFN}}$ cells, therefore we propose that increase in intracellular lipids
478 is due to enhanced uptake, although endogenous lipid synthesis cannot be
479 ruled out. Our findings that $\gamma\delta^{17}$ cell proliferation is boosted by cholesterol
480 treatment, and that these cells expand substantially in obese mice, provide
481 additional evidence that HFD causes a systemic increase in the $\gamma\delta^{17}$ subset,
482 consistent with previous findings in the skin⁴⁷ and lungs⁴⁸, and may provide a
483 mechanistic understanding for this expansion. Obesity is a known risk factor
484 for cancer and we previously demonstrated the link between obesity and
485 suppression of NK cell anti-tumour function⁴⁹. Given that $\gamma\delta^{17}$ cells have
486 strong pro-tumoural effects and we find this population to be expanded in
487 tumours of obese mice, this may represent an additional mechanism linking
488 cancer and obesity, whereby abundant lipids favor $\gamma\delta^{17}$ over $\gamma\delta^{\text{IFN}}$ cells to
489 support tumour growth.

490 Conversely, we found $\gamma\delta^{\text{IFN}}$ cells, from their thymic development to intra-
491 tumoural functions, to be boosted by glucose metabolism. Naturally, the large
492 consumption of glucose by tumour cells⁷ creates a major metabolic constraint
493 on $\gamma\delta^{\text{IFN}}$ TILs. Glucose restriction can impair T cell cytokine production^{5,6}, while
494 production of lactate by tumour cells performing aerobic glycolysis can inhibit
495 T cell proliferation and cytotoxic functions⁵⁰. Therefore, we do not conceive
496 glucose supplementation as an appropriate strategy to enhance endogenous
497 T cell (including $\gamma\delta^{\text{IFN}}$) responses *in vivo*. Instead, we suggest that it should be
498 considered in protocols used to expand/differentiate $\gamma\delta$ T cells *ex vivo* for
499 adoptive cell therapy. Such an “*in vitro* glucose boost” may enable stronger
500 anti-tumour activities (namely, IFN- γ production and cytotoxicity) upon T-cell
501 transfer, as suggested by our data using CD27⁺ $\gamma\delta^{\text{IFN}}$ cells in the breast cancer

502 model, although evaluation of the duration and long-term impact of this
503 “boost” requires further investigation in slower-growing tumour models.

504 While we did not dissect the mechanistic link between aerobic glycolysis and
505 IFN- γ production by CD27⁺ $\gamma\delta^{\text{IFN}}$ cells, previous studies on $\alpha\beta$ T cells have
506 shown that glycolysis controls (via the enzyme GAPDH) the translation of IFN-
507 γ mRNA⁵. Moreover, glycolysis was shown to be essential for the cytotoxic
508 activity of NK cells, namely their degranulation and Fas ligand expression,
509 upon engagement of NK cell receptors (NKR)s⁵¹. This is particularly
510 interesting when considering the potential of a human $\gamma\delta$ T cell product that we
511 developed for adoptive cell therapy of cancer, Delta One T (DOT) cells^{9,52,53}.
512 These V δ 1⁺ T cells are induced *in vitro* to express high levels of NKR)s that
513 enhance their cytotoxicity and IFN- γ production⁵²⁻⁵⁴. We therefore propose
514 that high dose glucose should be added to the DOT protocol as to further
515 increase their anti-tumour potential.

516 In sum, this study demonstrates that thymic differentiation of effector $\gamma\delta$ T cell
517 subsets, besides well-established epigenetic and transcriptional regulation,
518 includes divergent metabolic programming that is sustained in the periphery
519 and, in particular, in the TME. It further identifies distinct metabolic resources
520 that control the intra-tumoural activities of $\gamma\delta$ T cell subsets, with lipids
521 favoring $\gamma\delta^{17}$ cells and glucose boosting $\gamma\delta^{\text{IFN}}$ cells, which provides a new
522 metabolism-based angle for therapeutic intervention in cancer and possibly
523 other diseases.

524 **Methods**

525 **Ethics statement**

526 All mouse experiments performed in this study were evaluated and approved
527 by the institutional ethical committee (Instituto de Medicina Molecular Orbea),
528 the national competent authority (DGAV) under the license number 019069,
529 UK Home Office regulations and institutional guidelines under license number
530 70/8758 and by the Institutional Animal Care and Use Committee of Brigham
531 and Women's Hospital and Harvard Medical School, the Trinity College Dublin
532 ethics committee. Euthanasia was performed by CO₂ inhalation. Anesthesia
533 was performed by isoflurane inhalation.

534

535 **Mice and tumour cell lines**

536 C57Bl/6J WT mice and Myc-GFP mice (B6;129-Myc^{tm1Slek/J}) were purchased
537 from Charles River and Jackson Laboratories. PLZF-GFP (*Zbtb16*^{GFP}) mice
538 were generated in the laboratory of D. Sant'Angelo as described previously¹.
539 Mice were maintained under specific pathogen-free conditions. Standard food
540 and water were given *ad libitum*. Where indicated, mice were fed high fat diet
541 (HFD) (research diets) for 8 weeks. Mice were used at the foetal (embryonic
542 day 14-18), neonatal (1-5 days old) or adult (6-12 weeks old) stages.

543 The E0771 murine breast adenocarcinoma cells, MC38 murine colon
544 adenocarcinoma cells and B16.F10 melanoma cells were purchased from
545 ATCC (Manassas, VA). Cells were maintained in Dulbecco's Modified Eagle
546 Medium (DMEM) with 10% (vol/vol) FCS (Gibco; Thermo Fisher Scientific)
547 and 1% (vol/vol) penicillin/streptomycin (Sigma-Aldrich).

548

549 **Tumour transplantation *in vivo***

550 Mice were injected with 1 x 10⁶ E0771 tumour cells in fat pads, 1 x 10⁶ MC38
551 tumour cells or 2 x 10⁵ cells B16 tumour cells subcutaneously into the right
552 shaved flank. Tumour growth was measured every 2-3 days using calipers
553 and animals were sacrificed when tumours reached a diameter (D) of 15mm,
554 became ulcerous, or 1 or 2 weeks after tumour injection. Tumour size was

555 calculated using the following formula: $(D1)^2 \times (D2/2)$, D1 being the smaller
556 value of the tumour diameter. In some experiments, mice were fed with a
557 HFD (60% calories from lard) for 10 weeks prior to tumour injection and the
558 HFD was continued throughout the experiment.

559

560 **Comprehensive Lab Animal Monitoring System**

561 Indirect calorimetry data were recorded using a Promethion Metabolic Cage
562 System (Sable Systems) essentially as described previously². Mice were
563 housed individually in metabolic chambers under a 12h light/dark cycle at
564 room temperature (22°C) with free access to food and water. Mice were
565 acclimated for 24h in metabolic cages before recording calorimetric variables.
566 Mice were fed either a standard chow diet or a high fat (60%) diet ad libitum
567 for 12 weeks prior to being placed in the metabolic cages and were
568 maintained on either diet throughout the recording.

569

570 **Tissue processing and cell isolation**

571 Tumours were collected and digested with 1mg/mL collagenase Type I, 0.4
572 mg/mL collagenase Type IV (Worthington) and 10 µg/mL DNase I (Sigma-
573 Aldrich) for 30 minutes at 37°C. Cell suspension was then filtered through a
574 100 µm nylon cell strainer (Falcon/Corning). $\gamma\delta$ T cells were isolated by
575 scratching thymus, spleen and lymph node on a 70µm mesh. Lungs were
576 minced then homogenized in RPMI 1640 using a TissueLyser (Qiagen) and
577 filtered through 70µm mesh. Adipose tissue was processed as described
578 previously³. Red blood cells were lysed using RBC Lysis Buffer (Biolegend) or
579 ammonium chloride lysis buffer (made in-house). Single-cell suspensions of
580 foetal and neonatal thymocytes were obtained by gently homogenizing thymic
581 lobes followed by straining through 40µm strainers (BD).

582 For cell-sorting, $\gamma\delta$ T cells were pre-enriched by depletion of CD4⁺ and CD8⁺ T
583 cells, dendritic cells and B cells using biotinylated anti-CD4 (RM4-5), anti-CD8
584 (53-6.7), anti-CD11c (N14) and anti-CD19 (6D5) antibodies with anti-biotin
585 microbeads (Miltenyi Biotech) by QuadroMACS or $\gamma\delta$ T cells were purified

586 using TCR γ/δ T Cell Isolation Kit, mouse (Miltenyi Biotec). Cells were sorted
587 on a FACS Aria (BD Biosciences).

588

589 **Cell Culture**

590 CD27⁻ $\gamma\delta$ T cells were expanded *in vitro* as previously described⁴. This
591 protocol was adapted to expand CD27⁺ $\gamma\delta$ T cells by using 10ng/ml IL-2,
592 10ng/ml IL-15 and 20ng/ml IL-7. For downstream assays, $\gamma\delta$ T cells were
593 purified using TCR γ/δ T Cell Isolation Kit, mouse (Miltenyi Biotec). *Ex vivo*
594 cultures were performed using RPMI 1640 (Gibco) supplemented with 10%
595 heat-inactivated foetal bovine serum (Gibco), 1% penicillin/streptomycin, 1%
596 L-glutamine. For cytokine stimulation, cells were cultured with 10ng/ml IL-1 β
597 and IL-23 (Miltenyi Biotec) and/or IL-12 and IL-18 (BioLegend).

598 For short-term skin-draining-lymphocyte cultures, single-cell suspensions of
599 lymphocytes were isolated from skin-draining lymph nodes from adult B6
600 mice. Cells were resuspended in complete RPMI medium (RPMI-1640 with
601 10% FCS, 1% penicillin and streptomycin, and 2 mM L-glutamine). 1×10^6
602 lymphocytes in 500 μ l of complete medium were incubated for 48h in 48-well
603 plates either under control conditions or with the addition of 5-aminoimidazole-
604 4-carboxamide (AICAR; 1.6 mM; Sigma-Aldrich). Cells were subsequently
605 analysed by flow cytometry.

606

607 **Foetal Thymic Organ Cultures (FTOC)**

608 E15-E17 thymic lobes from B6 mice were cultured on nucleopore membrane
609 filter discs (Whatman) in FTOC medium (RPMI-1640 with 10% FCS, 1%
610 penicillin and streptomycin, 50 μ M β -mercaptoethanol (Invitrogen), and 2 mM
611 L-glutamine (Sigma-Aldrich)) for 6-12 days (unless otherwise indicated). In
612 some experiments 2-deoxyglucose (2-DG; 0.6 mM), fasentin (0.6 mM),
613 metformin (2 mM) or oligomycin (1 nM) were added to the cultures. All thymic
614 organ cultures were subsequently analysed by flow cytometry. In some
615 cultures, where concentration of glucose was manipulated, "basic" FTOC

616 medium (RPMI-1640 [-] glucose with 10% FCS, 1% penicillin and
617 streptomycin, 50 μ M β -mercaptoethanol (Invitrogen), and 2 mM L-glutamine
618 (Sigma-Aldrich)) was used, and glucose was added at 5mM for “low-glucose”
619 conditions or 25mM for “high-glucose” conditions.

620 In some experiments, anti-TCR δ antibody (GL3; 1 μ g/ml unless otherwise
621 indicated) was added to the cultures. Cultures containing antibody were
622 rested overnight in fresh FTOC medium before analysis. All thymic organ
623 cultures were subsequently analysed by flow cytometry.

624

625 **Manipulation of $\gamma\delta$ metabolic pathways *in vitro* and *in vivo***

626 Spleen and lymph nodes were harvested from C57Bl/6J mice. Cell
627 suspensions were stained with LIVE/DEAD Fixable Near-IR (Thermo Fisher
628 Scientific), anti-CD3 ϵ (145-2C11), anti-TCR δ (GL3), and anti-CD27 (LG.7F9)
629 for 15 minutes at 4°C. CD27 $^+$ and CD27 $^-$ $\gamma\delta$ T cells were FACS-sorted. CD27 $^+$
630 and CD27 $^-$ $\gamma\delta$ T cells were incubated on plate-bound anti-CD3 ϵ (145.2C11)
631 (10 μ g/mL) in the presence of IL-7 (50 μ g/mL) or IL-7 (50 μ g/mL), IL-1 β (10
632 μ g/mL) and IL-23 (10 μ g/mL), respectively. All cytokines were purchased from
633 Peprotech. Then, cells were cultured with 2-Deoxy-D-Glucose (2-DG; 2mM;
634 Sigma-Aldrich), high D-glucose (50mM; Sigma-Aldrich), galactose (20mM;
635 Sigma-Aldrich), Carbonyl cyanide 4-(trifluoromethoxy) phenylhydrazone
636 (FCCP; 1 μ M; Sigma-Aldrich) and cholesterol-loaded cyclodextrin (CLC;
637 5 μ g/mL) for 5h at 37°C for *in vitro* experiments.

638 For experiments *in vivo*, purified CD27 $^-$ and CD27 $^+$ $\gamma\delta$ T cells were incubated
639 (or not) for 5h with cholesterol-loaded cyclodextrin (5 μ g/mL) or with high D-
640 glucose (50mM; Sigma-Aldrich), respectively. 5 x 10 5 CD27 $^-$ or 1 x 10 6 CD27 $^+$
641 $\gamma\delta$ T cells were injected twice directly at the tumor site (1 $^{\text{st}}$ injection 7 days
642 after tumour inoculation and 2 $^{\text{nd}}$ injection 2 days later). Mice were analyzed 11
643 days after tumour cell injection.

644 For lipid depletion *in vivo*, mice were injected daily with 50mg/kg Orlistat i.p.
645 on days 6-9 after tumour injection, then tumour cell infiltrate was analysed on
646 day 10.

647 **Killing assays for CD27⁺ $\gamma\delta$ T cells *in vitro***

648 Purified CD27⁺ $\gamma\delta$ T cells were supplemented (or not) with high levels of
649 glucose (50mM; Sigma-Aldrich) for 5h at 37°C, 5% CO₂. Then, variable
650 numbers of CD27⁺ $\gamma\delta$ T cells were co-cultured with 5 x 10⁵ E0771 breast
651 cancer cells in complete RPMI Medium (minus D-Glucose). The killing
652 capacities of CD27⁺ $\gamma\delta$ T cells based on death of E0771 cells (Annexin V
653 staining) was assessed by flow cytometry after 24h.

654

655 **Flow cytometry**

656 $\gamma\delta$ T cells were analysed by flow cytometry using standard procedures. For
657 surface staining, cells were Fc-blocked with anti-CD16/32 (clone 93;
658 eBioscience) and incubated for 15 minutes at 4°C with antibodies and
659 LIVE/DEAD Fixable Near-IR (Thermo Fisher Scientific) or viability dye Zombie
660 NIR stain (BioLegend) in FACs buffer (PBS 1X, 10% FCS, 0.5M EDTA). Anti-
661 CD3 ϵ (145-2C11), anti-CD27 (LG.7F9), anti-CD25 (PC61), anti-CD73
662 (TY/11.8) and anti-V γ 2 (UC3-10A6) were purchased from eBioscience. Anti-
663 CD45 (30-F11), anti-TCR δ (GL3), anti-CD24 (M1/69), anti-V γ 1 (2.11), anti-V γ 4
664 (UC3-10A6), anti-V γ 5 (536) and anti-CD45RB (C363-16A) were purchased
665 from BioLegend and anti-CD44 (IM7) from BD Pharmingen. Cells were
666 washed with FACS buffer. For intracellular cytokine staining, cells were
667 stimulated with 50 μ g/mL phorbol 12-myristate 13-acetate (PMA; Sigma-
668 Aldrich) and 1 μ g/mL ionomycin (Sigma-Aldrich) for 3-4 hours at 37°C, 5%
669 CO₂ in the presence of 10 μ g/mL brefeldin-A (Sigma-Aldrich) and 2 μ M
670 monensin (eBioscience). Cells were fixed and permeabilized with Foxp3
671 staining kit (eBioscience/Thermo Fisher Scientific), according to the
672 manufacturer's instructions. Cells were incubated for 30 minutes at 4°C, with
673 the following antibodies from eBioscience: anti-IFN- γ (XMG1.2), anti-IL-17
674 (TC11-18H10.1), Ki67 (16A8), T-bet (4B10) and ROR γ t (B2D). For Annexin V
675 staining, Annexin V Kit (eBioscience) was used following manufacturer's
676 instructions.

677 The following dyes were purchased from Invitrogen and stained according to
678 manufacturer's instructions: Mitotracker™ Green FM, Tetramethylrhodamine
679 Methyl Ester Perchlorate (TMRM), HCS LipidTOX™ Red Neutral Lipid Stain.
680 Palmitate uptake was measured using 1μM Bodipy FL-C₁₆ (Invitrogen)
681 incubated for 10mins at 37°C. Cholesterol ester uptake was measured using
682 2μM Bodipy CholEsteryl FL-C₁₂ incubated for 1h at 37°C. Cholesterol content
683 was measured using 50μg/ml Filipin III (Sigma-Aldrich) incubated for 1h at
684 room temperature.

685 Flow cytometry analysis was performed with a FACS Fortessa, LSRII or
686 Canto II (BD Biosciences) and data analysed using FlowJo software (BD
687 Biosciences).

688

689 **Metabolism profile of cells**

690 Seahorse Metabolic Flux Analysis: Real-time analysis of oxygen consumption
691 rates (OCR) and extracellular-acidification rates (ECAR) of IFN-γ- and IL-17-
692 committed γδ T cells sorted from 5-day-old B6 pups and CD27^{+/-} γδ T cells
693 from spleen/lymph nodes expanded *in vitro* were assessed using the XFp
694 Extracellular Flux or Seahorse XFe-96 analyzers, respectively (Seahorse
695 Bioscience). Cells were added to a Seahorse XF96 Cell Culture Microplate
696 (Agilent), coated with Cell-Tak (Corning) to ensure adherence, and sequential
697 measurements of ECAR and OCR were performed in XF RPMI Seahorse
698 medium supplemented with glucose (10mM), glutamine (2mM), and sodium
699 pyruvate (1mM) following the addition of Oligomycin A (2μM), FCCP (2μM),
700 rotenone (1μM) plus antimycin A (1-4μM). Basal glycolysis, glycolytic
701 capacity, basal mitochondrial respiration and maximal mitochondrial
702 respiration were calculated. OCR and ECAR values were normalized to cell
703 number.

704

705 **SCENITH™**

706 Cells were plated at 20 × 10⁶ cells/ml in 96-well plates. After activation of γδ T
707 cells, cells were treated for 30 minutes at 37°C, 5% CO₂ with Control (Co), 2-

708 Deoxy-D-Glucose (DG; 100mM; Sigma-Aldrich), Oligomycin (O; 1 μ M; Sigma-
709 Aldrich) or a combination of both drugs (DGO). Puromycin (Puro, 10 μ g/ml;
710 Sigma-Aldrich) is added during 15 minutes at 37°C. SCENITH™ kit
711 (<http://www.scenith.com>) containing all reagents and protocols were kindly
712 provided by Dr. Rafael Argüello, (CIML). Cells were washed in cold PBS and
713 stained with primary conjugated antibodies against different surface markers
714 (as described above) for 15 minutes at 4°C in FACS buffer (PBS 1X 5% FCS,
715 2mM EDTA). After washing with FACS buffer, cells were fixed and
716 permeabilized using Cytotfix/Cytoperm™ (BD) following manufacturer's
717 instructions. Intracellular staining of puromycin using the anti-Puro monoclonal
718 antibody (1:600, Clone R4743L-E8) was performed by incubating cells during
719 30min at 4°C diluted in Permwash. Experimental duplicates were performed in
720 all conditions.

721

722 ***In vivo* glucose uptake**

723 2-NBDG (300 μ g diluted in PBS 1X; Cayman chemical) was injected i.v. in
724 C57Bl/6J mice; 15min later, cells from tumours were harvested.

725

726 **Assessment of mitochondrial morphology**

727 Mitochondrial membrane potential was measured using
728 tetramethylrhodamine, ethyl ester (TMRE; 100nM; Abcam) according to
729 manufacturer protocols. Following TMRE staining, carbonyl cyanide-4-
730 (trifluoromethoxy) phenylhydrazone (FCCP; 25 μ M; Abcam) was used as a
731 positive control for mitochondrial membrane depolarization. Total
732 mitochondrial mass was assessed using MitoTracker Green (Invitrogen)
733 according to manufacturer's instructions. All cells were subsequently analysed
734 by flow cytometry.

735

736 **Triglyceride Quantification**

737 Triglycerides (TAGs) were quantified from expanded $\gamma\delta$ T cells *in vitro* using
738 Picoprobe Triglyceride Quantification Assay Kit, Fluorometric (Abcam) and
739 absorbance measured using FLUOstar OPTIMA (BMG Labtech).

740

741

742 **RNA isolation and real-time PCR**

743 mRNA was prepared from FACS-sorted CD27⁺ and CD27⁻ $\gamma\delta$ T cells from WT
744 spleen and draining lymph nodes using High Pure RNA Isolation kit (Roche).
745 Reverse transcription was performed with random oligonucleotides
746 (Invitrogen). Results were normalized to actin mRNA. qPCR was performed
747 with SYBR Premix Ex Taq master mix (Takara) on an ABI ViiA7 cycler
748 (Applied Biosystems). The CT for the target gene was subtracted from the CT
749 for the endogenous reference, and the relative amount was calculated as
750 $2^{-\Delta\text{CT}}$.

751

752 **Imaging**

753 Thymocytes from B6 E15 thymic lobes cultured for 12 days were isolated and
754 stained for surface markers and then Mitotracker Green or TMRE (as
755 described above). All cells were subsequently analysed on an ImageStream[™]
756 Mark II imaging flow cytometer (Amnis); 30k events were saved from samples
757 and 1k positive events from compensation single color controls. Analysis was
758 performed using IDEAS® version 6.2.

759 For lipid droplet quantification, expanded $\gamma\delta$ T cells *in vitro* were stained with
760 LipidTOX red neutral lipid stain (Invitrogen) and Hoechst 33342 (Sigma-
761 Aldrich). Mitotracker Green FM (Invitrogen) was used to identify mitochondria.
762 Cells were mounted onto poly-L-lysine coated slides. Images were obtained
763 with a Zeiss LSM 800 confocal microscope using Zen 2.3 software (Zeiss)
764 and analyzed using ImageJ.

765

766 **RNA-sequencing and data processing**

767 Single-cell sequencing libraries were generated using the Chromium™ Single
768 Cell 5' Library and Gel Bead Kit (10X Genomics) according to the
769 manufacturer's instructions. Data was analysed using the R package Seurat
770 v2.3^{5,6}.

771 UMI counts were normalized using regularized negative binomial regression
772 with the SCTransform package⁷. For downstream analysis of normalized data
773 principal component analysis (PCA) was performed using n=50 dimensions
774 and PCA variability was determined using an Elbow plot. Differential gene
775 expression analysis and GSEA was performed using the MAST and fgsea
776 packages^{6,7}. Pathways and gene lists for gene set enrichment analysis were
777 obtained using the misgdbR package from Molecular Signatures database
778 (MSigDB)^{8,9}. Adaptively-thresholded Low Rank Approximation (ALRA) from
779 the Seurat wrappers package was performed to correct for drop-out values for
780 visualization of leading-edge and differentially expressed genes identified by
781 MAST¹⁰. The accession codes for single-cell RNA sequencing
782 are GSE150585 and GSE156782.

783 All downstream analysis was performed using R v.3.6.3 and RStudio Desktop
784 1.2.5001 on an Ubuntu 19.10 linux (64 bit) system using the following R
785 packages and libraries: dplyr v.0.8.5, fgsea v.1.12.0, ggplot2 v.3.3.0, MAST
786 v.1.12.0, SCTransform v.0.2.1, Seurat v.3.1.4, SeuratWrappers v.0.1.0, uwot
787 v.0.1.8 and viridis v.0.5.1.

788

789 **Statistical analysis**

790 Statistical analysis was performed using GraphPad Prism software using non-
791 parametric two-tailed Mann-Whitney test or, if both groups followed a normal
792 distribution (tested by D'Agostino and Pearson normality test), using two-
793 tailed unpaired Student *t* test or one-way analysis of variance. All data are
794 presented as means ± standard error of mean (SEM) or standard deviation
795 (SD). **p* < 0.05; ***p* < 0.01; ****p* < 0.001, ****<0.0001.

796

797 1. Lynch, L. *et al.* Regulatory iNKT cells lack expression of the transcription
798 factor PLZF and control the homeostasis of T reg cells and macrophages in

- 799 adipose tissue. *Nat. Immunol.* **16**, 85–95 (2015).
- 800 2. Vu, J. P. *et al.* Long-Term Intake of a High-Protein Diet Affects Body
801 Phenotype, Metabolism, and Plasma Hormones in Mice. *J. Nutr.* **147**, 2243–
802 2251 (2017).
- 803 3. Kohlgruber, A. C. *et al.* $\gamma\delta$ T cells producing interleukin-17A regulate adipose
804 regulatory T cell homeostasis and thermogenesis. *Nat. Immunol.* **19**, (2018).
- 805 4. McKenzie, D. R. *et al.* IL-17-producing $\gamma\delta$ T cells switch migratory patterns
806 between resting and activated states. *Nat. Commun.* **8**, 15632 (2017).
- 807 5. Butler, A., Hoffman, P., Smibert, P., Papalexi, E. & Satija, R. Integrating
808 single-cell transcriptomic data across different conditions, technologies, and
809 species. *Nat. Biotechnol.* **36**, 411–420 (2018).
- 810 6. Stuart, T. *et al.* Comprehensive Integration of Single-Cell Data Resource
811 Comprehensive Integration of Single-Cell Data. *Cell* **177**, (2019).
- 812 7. Hafemeister, C. & Satija, R. Normalization and variance stabilization of single-
813 cell RNA-seq data using regularized negative binomial regression. *Genome*
814 *Biol.* **20**, 296 (2019).
- 815 8. Subramanian, A. *et al.* Gene set enrichment analysis: A knowledge-based
816 approach for interpreting genome-wide expression profiles. *Proc. Natl. Acad.*
817 *Sci. U. S. A.* **102**, 15545–15550 (2005).
- 818 9. Liberzon, A. *et al.* Databases and ontologies Molecular signatures database
819 (MSigDB) 3.0. *Bioinforma. Appl. NOTE* **27**, 1739–1740 (2011).
- 820 10. Linderman, G. C., Zhao, J. & Kluger, Y. Zero-preserving imputation of scRNA-
821 seq data using low-rank approximation. *bioRxiv* 397588 (2018).
822 doi:10.1101/397588
- 823
- 824
- 825

826 **Acknowledgments**

827 We are grateful for the valuable assistance of the staff of the flow cytometry,
828 bioimaging and animal facilities at our Institutions. We thank Ana Magalhães,
829 Julie Ribot, Karine Serre, and Natacha Sousa (iMM) for technical suggestions
830 and administrative help. This work was supported by the European Research
831 Council (CoG_646701 to B.S.-S.; Stg_679173 to L.L.), Wellcome Trust
832 (092973/Z/10/Z to D.J.P.), Science Foundation Ireland (SFI) (16/FRL/3865 to
833 L.L), NIH (NS115064, HG008155, AG062377 to M.K), R01 AI134861,
834 Biotechnology and Biological Sciences Research Council (BBSRC) UK
835 (BB/R017808/1 to D.J.P) and Astrazeneca (Prémio FAZ Ciência 2019 to B.S.-
836 S. and N.L.). N.L is supported by a post-doctoral fellowship from EMBO
837 (ALTF 752-2018); S.M. was supported by a studentship from Medical
838 Research Council (MRC) UK; G.F. is supported by a European Commission
839 Marie Skłodowska-Curie Individual Fellowship (ref. 752932); and A.D, S.C.
840 L.D and H.P are supported by Irish Research Council fellowships.

841

842 **Author contributions**

843 N.L, C.M, S.M and M.R performed most of the experiments and analyzed the
844 data. G.F. designed and performed some experiments. N.S., A.K., L.D., H.K.,
845 A.D., S.C., H.P. R.L. and C.C. provided technical assistance in some
846 experiments. M.K. and L.A performed bioinformatic analysis and M.B provided
847 reagents, materials and support. R.A. provided key assistance with the
848 SCENITH™ methodology. B.S.-S., D.P and L.L conceived and supervised the
849 study. N.L, C.M., B.S.-S., D.J.P. and L.L. wrote the manuscript.

850

851

852

853 **References**

- 854 1 Buck, M. D., Sowell, R. T., Kaech, S. M. & Pearce, E. L. Metabolic
855 Instruction of Immunity. *Cell* **169**, 570-586,
856 doi:10.1016/j.cell.2017.04.004 (2017).
- 857 2 Almeida, L., Lochner, M., Berod, L. & Sparwasser, T. Metabolic
858 pathways in T cell activation and lineage differentiation. *Semin*
859 *Immunol* **28**, 514-524, doi:10.1016/j.smim.2016.10.009 (2016).
- 860 3 Geltink, R. I. K., Kyle, R. L. & Pearce, E. L. Unraveling the Complex
861 Interplay Between T Cell Metabolism and Function. *Annu Rev Immunol*
862 **36**, 461-488, doi:10.1146/annurev-immunol-042617-053019 (2018).
- 863 4 Cham, C. M., Driessens, G., O'Keefe, J. P. & Gajewski, T. F. Glucose
864 deprivation inhibits multiple key gene expression events and effector
865 functions in CD8+ T cells. *Eur J Immunol* **38**, 2438-2450,
866 doi:10.1002/eji.200838289 (2008).
- 867 5 Chang, C. H. *et al.* Posttranscriptional control of T cell effector function
868 by aerobic glycolysis. *Cell* **153**, 1239-1251,
869 doi:10.1016/j.cell.2013.05.016 (2013).
- 870 6 Chang, C. H. *et al.* Metabolic Competition in the Tumor
871 Microenvironment Is a Driver of Cancer Progression. *Cell* **162**, 1229-
872 1241, doi:10.1016/j.cell.2015.08.016 (2015).
- 873 7 O'Sullivan, D., Sanin, D. E., Pearce, E. J. & Pearce, E. L. Metabolic
874 interventions in the immune response to cancer. *Nat Rev Immunol* **19**,
875 324-335, doi:10.1038/s41577-019-0140-9 (2019).
- 876 8 Silva-Santos, B., Mensurado, S. & Coffelt, S. B. gammadelta T cells:
877 pleiotropic immune effectors with therapeutic potential in cancer. *Nat*
878 *Rev Cancer* **19**, 392-404, doi:10.1038/s41568-019-0153-5 (2019).
- 879 9 Sebestyen, Z., Prinz, I., Dechanet-Merville, J., Silva-Santos, B. &
880 Kuball, J. Translating gammadelta (gammadelta) T cells and their
881 receptors into cancer cell therapies. *Nat Rev Drug Discov* **19**, 169-184,
882 doi:10.1038/s41573-019-0038-z (2020).

- 883 10 Chien, Y. H., Meyer, C. & Bonneville, M. gammadelta T cells: first line
884 of defense and beyond. *Annu Rev Immunol* **32**, 121-155,
885 doi:10.1146/annurev-immunol-032713-120216 (2014).
- 886 11 Hayday, A. C. Gammadelta T cells and the lymphoid stress-
887 surveillance response. *Immunity* **31**, 184-196,
888 doi:10.1016/j.immuni.2009.08.006 (2009).
- 889 12 Hayday, A. C. gammadelta T Cell Update: Adaptate Orchestrators of
890 Immune Surveillance. *J Immunol* **203**, 311-320,
891 doi:10.4049/jimmunol.1800934 (2019).
- 892 13 Ravens, S. *et al.* Human gammadelta T cells are quickly reconstituted
893 after stem-cell transplantation and show adaptive clonal expansion in
894 response to viral infection. *Nat Immunol* **18**, 393-401,
895 doi:10.1038/ni.3686 (2017).
- 896 14 Kohlgruber, A. C. *et al.* gammadelta T cells producing interleukin-17A
897 regulate adipose regulatory T cell homeostasis and thermogenesis. *Nat*
898 *Immunol* **19**, 464-474, doi:10.1038/s41590-018-0094-2 (2018).
- 899 15 Ribeiro, M. *et al.* Meningeal gammadelta T cell-derived IL-17 controls
900 synaptic plasticity and short-term memory. *Sci Immunol* **4**,
901 doi:10.1126/sciimmunol.aay5199 (2019).
- 902 16 Papotto, P. H., Ribot, J. C. & Silva-Santos, B. IL-17(+) gammadelta T
903 cells as kick-starters of inflammation. *Nat Immunol* **18**, 604-611,
904 doi:10.1038/ni.3726 (2017).
- 905 17 Jensen, K. D. *et al.* Thymic selection determines gammadelta T cell
906 effector fate: antigen-naive cells make interleukin-17 and antigen-
907 experienced cells make interferon gamma. *Immunity* **29**, 90-100,
908 doi:10.1016/j.immuni.2008.04.022 (2008).
- 909 18 Ribot, J. C. *et al.* CD27 is a thymic determinant of the balance between
910 interferon-gamma- and interleukin 17-producing gammadelta T cell
911 subsets. *Nat Immunol* **10**, 427-436, doi:10.1038/ni.1717 (2009).
- 912 19 Sumaria, N., Grandjean, C. L., Silva-Santos, B. & Pennington, D. J.
913 Strong TCRgammadelta Signaling Prohibits Thymic Development of IL-

- 914 17A-Secreting gammadelta T Cells. *Cell Rep* **19**, 2469-2476,
915 doi:10.1016/j.celrep.2017.05.071 (2017).
- 916 20 Munoz-Ruiz, M. *et al.* TCR signal strength controls thymic
917 differentiation of discrete proinflammatory gammadelta T cell subsets.
918 *Nat Immunol* **17**, 721-727, doi:10.1038/ni.3424 (2016).
- 919 21 Munoz-Ruiz, M., Sumaria, N., Pennington, D. J. & Silva-Santos, B.
920 Thymic Determinants of gammadelta T Cell Differentiation. *Trends*
921 *Immunol* **38**, 336-344, doi:10.1016/j.it.2017.01.007 (2017).
- 922 22 Silva-Santos, B., Serre, K. & Norell, H. gammadelta T cells in cancer.
923 *Nat Rev Immunol* **15**, 683-691, doi:10.1038/nri3904 (2015).
- 924 23 Argüello, R., Combes AJ., Char, R., Gigan, JP., Baaziz, Al., Bousiquot,
925 E., Camosseto, V., Samad, B., Tsui, J., Yan, P., Boissoneau, S.,
926 Figarella-Branger, D., Gatti, E., Tabouret, E., Krummel, MF and Pierre,
927 P. SCENITH: A flow cytometry based method for functional profiling
928 energy metabolism with single cell resolution. *Cell Metabolism (in*
929 *Press)* (2020).
- 930 24 Gleyzer, N., Vercauteren, K. & Scarpulla, R. C. Control of mitochondrial
931 transcription specificity factors (TFB1M and TFB2M) by nuclear
932 respiratory factors (NRF-1 and NRF-2) and PGC-1 family coactivators.
933 *Mol Cell Biol* **25**, 1354-1366, doi:10.1128/MCB.25.4.1354-1366.2005
934 (2005).
- 935 25 Scarpulla, R. C. Nuclear control of respiratory chain expression in
936 mammalian cells. *J Bioenerg Biomembr* **29**, 109-119,
937 doi:10.1023/a:1022681828846 (1997).
- 938 26 Dang, C. V. *et al.* The c-Myc target gene network. *Semin Cancer Biol*
939 **16**, 253-264, doi:10.1016/j.semcancer.2006.07.014 (2006).
- 940 27 Guo, Q. M. *et al.* Identification of c-myc responsive genes using rat
941 cDNA microarray. *Cancer Res* **60**, 5922-5928 (2000).
- 942 28 In, T. S. H. *et al.* HEB is required for the specification of fetal IL-17-
943 producing gammadelta T cells. *Nat Commun* **8**, 2004,
944 doi:10.1038/s41467-017-02225-5 (2017).

- 945 29 Coffey, F. *et al.* The TCR ligand-inducible expression of CD73 marks
946 gammadelta lineage commitment and a metastable intermediate in
947 effector specification. *J Exp Med* **211**, 329-343,
948 doi:10.1084/jem.20131540 (2014).
- 949 30 Turchinovich, G. & Hayday, A. C. Skint-1 identifies a common
950 molecular mechanism for the development of interferon-gamma-
951 secreting versus interleukin-17-secreting gammadelta T cells. *Immunity*
952 **35**, 59-68, doi:10.1016/j.immuni.2011.04.018 (2011).
- 953 31 Lu, Y., Cao, X., Zhang, X. & Kovalovsky, D. PLZF Controls the
954 Development of Fetal-Derived IL-17+Vgamma6+ gammadelta T Cells.
955 *J Immunol* **195**, 4273-4281, doi:10.4049/jimmunol.1500939 (2015).
- 956 32 Tan, L. *et al.* Single-Cell Transcriptomics Identifies the Adaptation of
957 Scart1(+) Vgamma6(+) T Cells to Skin Residency as Activated Effector
958 Cells. *Cell Rep* **27**, 3657-3671 e3654, doi:10.1016/j.celrep.2019.05.064
959 (2019).
- 960 33 McCully, M. L. *et al.* Skin Metabolites Define a New Paradigm in the
961 Localization of Skin Tropic Memory T Cells. *J Immunol* **195**, 96-104,
962 doi:10.4049/jimmunol.1402961 (2015).
- 963 34 Bartz, R. *et al.* Lipidomics reveals that adiposomes store ether lipids
964 and mediate phospholipid traffic. *J Lipid Res* **48**, 837-847,
965 doi:10.1194/jlr.M600413-JLR200 (2007).
- 966 35 Le Goffe, C., Vallette, G., Jarry, A., Bou-Hanna, C. & Laboissee, C. L.
967 The in vitro manipulation of carbohydrate metabolism: a new strategy
968 for deciphering the cellular defence mechanisms against nitric oxide
969 attack. *Biochem J* **344 Pt 3**, 643-648, doi:10.1042/0264-6021:3440643
970 (1999).
- 971 36 Bustamante, E. & Pedersen, P. L. High aerobic glycolysis of rat
972 hepatoma cells in culture: role of mitochondrial hexokinase. *Proc Natl*
973 *Acad Sci U S A* **74**, 3735-3739, doi:10.1073/pnas.74.9.3735 (1977).

- 974 37 Buck, M. D., O'Sullivan, D. & Pearce, E. L. T cell metabolism drives
975 immunity. *J Exp Med* **212**, 1345-1360, doi:10.1084/jem.20151159
976 (2015).
- 977 38 Menk, A. V. *et al.* Early TCR Signaling Induces Rapid Aerobic
978 Glycolysis Enabling Distinct Acute T Cell Effector Functions. *Cell Rep*
979 **22**, 1509-1521, doi:10.1016/j.celrep.2018.01.040 (2018).
- 980 39 Shin, B. *et al.* Mitochondrial Oxidative Phosphorylation Regulates the
981 Fate Decision between Pathogenic Th17 and Regulatory T Cells. *Cell*
982 *Rep* **30**, 1898-1909 e1894, doi:10.1016/j.celrep.2020.01.022 (2020).
- 983 40 Di Luccia, B., Gilfillan, S., Cella, M., Colonna, M. & Huang, S. C. ILC3s
984 integrate glycolysis and mitochondrial production of reactive oxygen
985 species to fulfill activation demands. *J Exp Med* **216**, 2231-2241,
986 doi:10.1084/jem.20180549 (2019).
- 987 41 Schmolka, N. *et al.* Epigenetic and transcriptional signatures of stable
988 versus plastic differentiation of proinflammatory gammadelta T cell
989 subsets. *Nat Immunol* **14**, 1093-1100, doi:10.1038/ni.2702 (2013).
- 990 42 Schmolka, N., Wencker, M., Hayday, A. C. & Silva-Santos, B.
991 Epigenetic and transcriptional regulation of gammadelta T cell
992 differentiation: Programming cells for responses in time and space.
993 *Semin Immunol* **27**, 19-25, doi:10.1016/j.smim.2015.01.001 (2015).
- 994 43 Gentles, A. J. *et al.* The prognostic landscape of genes and infiltrating
995 immune cells across human cancers. *Nat Med* **21**, 938-945,
996 doi:10.1038/nm.3909 (2015).
- 997 44 Legut, M., Cole, D. K. & Sewell, A. K. The promise of gammadelta T
998 cells and the gammadelta T cell receptor for cancer immunotherapy.
999 *Cell Mol Immunol* **12**, 656-668, doi:10.1038/cmi.2015.28 (2015).
- 1000 45 Baenke, F., Peck, B., Miess, H. & Schulze, A. Hooked on fat: the role
1001 of lipid synthesis in cancer metabolism and tumour development. *Dis*
1002 *Model Mech* **6**, 1353-1363, doi:10.1242/dmm.011338 (2013).

- 1003 46 Ma, X. *et al.* Cholesterol Induces CD8(+) T Cell Exhaustion in the
1004 Tumor Microenvironment. *Cell Metab* **30**, 143-156 e145,
1005 doi:10.1016/j.cmet.2019.04.002 (2019).
- 1006 47 Nakamizo, S. *et al.* High fat diet exacerbates murine psoriatic
1007 dermatitis by increasing the number of IL-17-producing gammadelta T
1008 cells. *Sci Rep* **7**, 14076, doi:10.1038/s41598-017-14292-1 (2017).
- 1009 48 Goldberg, E. L. *et al.* Ketogenic diet activates protective gammadelta T
1010 cell responses against influenza virus infection. *Sci Immunol* **4**,
1011 doi:10.1126/sciimmunol.aav2026 (2019).
- 1012 49 Michelet, X. *et al.* Metabolic reprogramming of natural killer cells in
1013 obesity limits antitumor responses. *Nat Immunol* **19**, 1330-1340,
1014 doi:10.1038/s41590-018-0251-7 (2018).
- 1015 50 Fischer, K. *et al.* Inhibitory effect of tumor cell-derived lactic acid on
1016 human T cells. *Blood* **109**, 3812-3819, doi:10.1182/blood-2006-07-
1017 035972 (2007).
- 1018 51 Wang, Z. *et al.* Glycolysis and Oxidative Phosphorylation Play Critical
1019 Roles in Natural Killer Cell Receptor-Mediated Natural Killer Cell
1020 Functions. *Front Immunol* **11**, 202, doi:10.3389/fimmu.2020.00202
1021 (2020).
- 1022 52 Almeida, A. R. *et al.* Delta One T Cells for Immunotherapy of Chronic
1023 Lymphocytic Leukemia: Clinical-Grade Expansion/Differentiation and
1024 Preclinical Proof of Concept. *Clin Cancer Res* **22**, 5795-5804,
1025 doi:10.1158/1078-0432.CCR-16-0597 (2016).
- 1026 53 Di Lorenzo, B. *et al.* Broad Cytotoxic Targeting of Acute Myeloid
1027 Leukemia by Polyclonal Delta One T Cells. *Cancer Immunol Res* **7**,
1028 552-558, doi:10.1158/2326-6066.CIR-18-0647 (2019).
- 1029 54 Correia, D. V. *et al.* Differentiation of human peripheral blood Vdelta1+
1030 T cells expressing the natural cytotoxicity receptor NKp30 for
1031 recognition of lymphoid leukemia cells. *Blood* **118**, 992-1001,
1032 doi:10.1182/blood-2011-02-339135 (2011).
- 1033

1034

1035

1036 **Figure Legends**

1037 **Figure 1. Intra-tumoural $\gamma\delta$ T cell subsets display distinct metabolic**
1038 **profiles.**

1039 **(a)** Experimental design: E0771 breast or MC38 colon cancer cell lines were
1040 injected in WT mice; 6 and 15 days later, tumours were extracted for
1041 metabolic analysis of $\gamma\delta$ T cells using SCENITH™. Inhibitors for different
1042 metabolic pathways were added for 30min followed by an incubation of 15min
1043 with puromycin. Mean fluorescence intensity (MFI) of puromycin is analyzed
1044 by flow cytometry in $\gamma\delta^{17}$ and $\gamma\delta^{\text{IFN}}$ subpopulations for each condition. **(b-e)**
1045 Puromycin MFI of $\gamma\delta^{17}$ and $\gamma\delta^{\text{IFN}}$ T cells from E0771 **(b,d)** and MC38 **(c,e)**
1046 tumour-bearing mice in control conditions (Co) or after the addition of 2-
1047 deoxy-D-glucose (DG), oligomycin (O) or both inhibitors (DGO). Graph shows
1048 the percentage of glucose dependence, mitochondrial dependence, glycolytic
1049 capacity and fatty acid and amino acid oxidation (FaaO) capacity of tumour-
1050 infiltrating $\gamma\delta^{17}$ and $\gamma\delta^{\text{IFN}}$ cells isolated either 6 **(d,e)** or 15 **(b,c)** days after
1051 cancer cell line injection. Data are representative of two independent
1052 experiments (n=5 mice per group in each experiment). pi: post-injection.
1053 $\gamma\delta^{17}$ and $\gamma\delta^{\text{IFN}}$ T cells represents IL-17 and IFN- γ -producing $\gamma\delta$ T cells,
1054 respectively. Error bars show mean \pm SEM, *p < 0.05; **p < 0.01; ****<0.0001
1055 using unpaired Student's t-test.

1056

1057 **Figure 2: Peripheral $\gamma\delta$ T cell subsets show different mitochondrial and**
1058 **metabolic phenotypes.**

1059 **(a)** Representative plots (left) and summary graphs (right) of the MFI of
1060 mitotracker and tetramethylrhodamine methyl ester (TMRM) in $\gamma\delta^{27-}$ ($\gamma\delta^{17}$) and
1061 $\gamma\delta^{27+}$ ($\gamma\delta^{\text{IFN}}$) T cells *ex vivo* from LNs of C57BL/6 mice (n=7; data pooled from
1062 2 experiments). **(b)** Representative confocal images (left) of $\gamma\delta^{17}$ and $\gamma\delta^{\text{IFN}}$ T
1063 cells stained with mitotracker (green) and Hoechst 33342 (blue). Scale bar
1064 represents 5 μ M. Analysis of mitotracker staining relative to cell size (right) in
1065 $\gamma\delta^{17}$ and $\gamma\delta^{\text{IFN}}$ cells *ex vivo*. Relative mitotracker was calculated by dividing the
1066 MFI of mitotracker by the MFI of FSC-A and multiplying by 100 (n=7, data

1067 pooled from 2 independent experiments). **(c)** Tetramethylrhodamine ethyl
1068 ester (TMRE) MFI of $\gamma\delta^{17}$ and $\gamma\delta^{\text{IFN}}$ T cells from skin draining LNs, mesenteric
1069 LNs, spleen and liver of WT mice. Data are representative of 3 independent
1070 experiments (n=3 mice per group and experiment). **(d)** Seahorse analysis of
1071 extracellular acidification rate (ECAR) and oxygen consumption rate (OCR) of
1072 $\gamma\delta^{17}$ and $\gamma\delta^{\text{IFN}}$ T cells (expanded *in vitro*) from LNs ($\gamma\delta^{17}$ n=2, $\gamma\delta^{\text{IFN}}$ n=5, data
1073 representative of 3 independent experiments). **(e)** Energy map showing ECAR
1074 vs OCR of $\gamma\delta^{17}$ and $\gamma\delta^{\text{IFN}}$ T cells. Each symbol represents average basal
1075 metabolism. **(f)** Basal glycolytic rate, glycolytic capacity and basal OxPhos of
1076 $\gamma\delta^{17}$ (n=3) and $\gamma\delta^{\text{IFN}}$ (n=8) cell subsets (data pooled from 2 independent
1077 experiments). **(g)** Percentage of glucose dependence, mitochondrial
1078 dependence, glycolytic capacity and fatty acid and amino acid oxidation
1079 (FaaO) capacity of $\gamma\delta^{17}$ and $\gamma\delta^{\text{IFN}}$ cells from spleen and draining lymph nodes
1080 (dLNs). Data are representative of three independent experiments (n=5 mice
1081 per group and per experiment). **(h,i)** OxPhos-related genes (*Ndufa11*,
1082 *Ndufa13*, *Sdha*, *Cox6a1*, *Cox7a1*, *Cox15*, *Nrf1*) and glycolysis-related genes
1083 (*Pgm1*, *Pgm2*, *Gpi1*, *Pgam1*, *Myc*) were measured by qPCR in purified $\gamma\delta^{17}$
1084 (n=4) and $\gamma\delta^{\text{IFN}}$ (n=4) T cells from spleen and dLN from WT mice. **(j)**
1085 Representative plot (left) and percentages (right) of Myc-GFP+ $\gamma\delta^{17}$ and $\gamma\delta^{\text{IFN}}$
1086 T cells from LNs of Myc-GFP reporter mice (n=2). Error bars show
1087 mean \pm SEM or SD, *p < 0.05; **p < 0.01; ***p < 0.001, ****p < 0.0001 using
1088 unpaired Student's t-test.

1089

1090 **Figure 3: $\gamma\delta$ T cell subsets are metabolically programmed in the thymus.**

1091 **(a)** Puromycin MFI of $\gamma\delta^{17}$ (CD44^{hi}CD45RB⁻) and $\gamma\delta^{\text{IFN}}$ (CD44⁺CD45RB⁺) T
1092 cells from WT adult thymus in resting conditions (Co) and after the addition of
1093 2-deoxy-D-glucose (DG), oligomycin (O) or both (DGO). Histogram (right)
1094 shows the percentage of glucose dependency (white), mitochondrial
1095 dependency (blue), glycolytic capacity (red) and fatty acid and amino acid
1096 oxidation (FaaO) capacity (purple) of thymic $\gamma\delta^{17}$ and $\gamma\delta^{\text{IFN}}$ cells. Data are
1097 representative of two independent experiments (n=5 mice per group and per
1098 experiment). **(b)** Histograms shows the percentage of glucose dependency

1099 (white), mitochondrial dependency (blue), glycolytic capacity (red) and fatty
1100 acid and amino acid oxidation (FaaO) capacity (purple) of $\gamma\delta^{17}$ and $\gamma\delta^{\text{IFN}}$ T
1101 cells from WT newborn thymus (d3). Data are representative of three
1102 independent experiments (n=6 mice per group and per experiment). **(c)** Flow
1103 cytometry profile and Tetramethylrhodamine ethyl ester (TMRE) MFI of thymic
1104 $\gamma\delta^{24+}$ precursors treated or not with FCCP. Data are representative of 3
1105 independent experiments (data points represent at least 4 lobes pooled per
1106 group and per experiment). **(d)** Flow cytometry profiles and TMRE MFI of
1107 thymic $\gamma\delta^{\text{TN}}$ (CD44⁻CD45RB⁻), $\gamma\delta^{17}$ (CD44^{hi}CD45RB⁻) and $\gamma\delta^{\text{IFN}}$
1108 (CD44⁺CD45RB⁺) cells treated or not with FCCP. Data are representative of 3
1109 independent experiments (data points represent at least 4 lobes pooled per
1110 group and per experiment). **(e)** Imagestream analysis of $\gamma\delta^{17}$ and $\gamma\delta^{\text{IFN}}$ cells
1111 stained with either mitotracker green or TMRE. Data are representative of 2
1112 independent experiments. **(f)** O₂ consumption rates (OCR) of $\gamma\delta^{17}$ and $\gamma\delta^{\text{IFN}}$
1113 cells were measured by Seahorse analysis in real-time under basal conditions
1114 and in response to indicated mitochondrial inhibitors. **(g)** Histograms show
1115 maximal respiration potential and spare respiratory capacity by measuring
1116 oxygen consumption rates (OCR) of $\gamma\delta^{17}$ and $\gamma\delta^{\text{IFN}}$ cells from thymuses of 5-
1117 day old B6 pups. Data are representative of 3 independent experiments
1118 (pooled thymic lobes from n>10 mice per group per experiment). **(h-j)** Flow
1119 cytometry profiles of thymic $\gamma\delta^{\text{TN}}$, $\gamma\delta^{17}$ and $\gamma\delta^{\text{IFN}}$ cells from 7-day FTOC of E15
1120 thymic lobes either with media containing low (5mM) or high (25mM) glucose
1121 **(h)**, or with or without 2-deoxy-d-glucose (2-DG) **(i)** or metformin **(j)**.
1122 Histograms show the number of $\gamma\delta^{17}$ cells and $\gamma\delta^{17}/\gamma\delta^{\text{IFN}}$ cell ratio. Data are
1123 representative of 2 **(h)** or 3 **(i-j)** independent experiments (at least 4 lobes
1124 pooled per group per experiment). Error bars show mean \pm SEM or SD,
1125 *p < 0.05, **p < 0.01, ***p < 0.001, ****p < 0.0001 using unpaired Student's t-
1126 test.

1127

1128 **Figure 4: Distinct mitochondrial activities underlie effector fate of thymic**
1129 **$\gamma\delta$ T cell progenitors.**

1130 **(a,b)** Flow cytometry profiles and percentage of thymic $\gamma\delta^{17}$ and $\gamma\delta^{\text{IFN}}$ cell
1131 output from post-sorted TMRE^{lo} and TMRE^{hi} $\gamma\delta^{\text{TN}}$ cells **(a)** or $\gamma\delta^{24+}$ cells **(b)**
1132 after 5-day culture on OP9DL1 cells. Data are representative of 3 independent
1133 experiments (n = 4 mice pooled per group per experiment). **(c)** Percentage of
1134 V γ 1⁺ and V γ 4⁺ cells in TMRE^{lo} and TMRE^{hi} $\gamma\delta^{24+}$ and $\gamma\delta^{24-}$ subsets. Data are
1135 representative of 3 independent experiments (cells sorted from n=4 mice
1136 pooled per group per experiment). **(d)** TMRE MFI of thymic $\gamma\delta^{\text{TN}}$ (CD44⁻
1137 CD45RB⁻), CD24⁻CD44⁻CD45RB⁺ $\gamma\delta$ T cells and $\gamma\delta^{\text{IFN}}$ cells (CD44⁺CD45RB⁺)
1138 from 6-day FTOC of E17 B6 thymic lobes. **(e)** TMRE staining in CD24⁻CD73⁺,
1139 CD24⁻CD73⁻, CD24⁺CD73⁺ and CD24⁺CD73⁻ $\gamma\delta$ T cells from 7-day FTOC of
1140 E15 B6 thymic lobes. **(f)** TMRE staining in CD25⁻CD24⁺ ($\gamma\delta^{24+}$ cells), CD25^{med},
1141 CD25^{hi} and V γ 5⁺ $\gamma\delta$ progenitors from E15 thymus. **(g)** Flow cytometry profiles
1142 of thymic $\gamma\delta^{\text{TN}}$, $\gamma\delta^{17}$ and $\gamma\delta^{\text{IFN}}$ cells from 6-day FTOC of E17 B6 thymic lobes
1143 stimulated or not with anti-TCR δ mAb (GL3; 1 μ g/ml). Graph shows
1144 percentage of $\gamma\delta^{17}$ and $\gamma\delta^{\text{IFN}}$ cells in each condition. **(h)** FACS-sorted
1145 $\gamma\delta^{24+}$ TMRE^{hi} cells from E17 thymi were cultured (or not) for 5h with different
1146 concentrations (as indicated) of anti-TCR δ mAb (GL3). TMRE levels were
1147 analysed by flow cytometry in $\gamma\delta^{24-}$ and $\gamma\delta^{24+}$ cells. Data are representative of
1148 3 independent experiments (n=4 mice pooled per group per experiment). **(i)**
1149 Experimental design for single-cell RNAseq (10x Genomics) on TMRE^{lo} and
1150 TMRE^{hi} $\gamma\delta^{24+}$ cells from E15 + 2d FTOC. **(j)** Clustering of single TMRE^{lo} and
1151 TMRE^{hi} $\gamma\delta^{24+}$ cells using UMAP. **(k)** GO term analysis of genes upregulated in
1152 TMRE^{lo} versus TMRE^{hi} $\gamma\delta^{24+}$ cells. **(l)** Heatmap of differentially upregulated
1153 genes from comparison of TMRE^{lo} and TMRE^{hi} $\gamma\delta^{24+}$ cells. Genes are grouped
1154 in relation to their function in either OxPhos or glucose metabolism. Error bars
1155 show mean \pm SD, *p < 0.05, **p < 0.01, ***p < 0.001, ****p < 0.0001 using
1156 unpaired Student's t-test.

1157

1158 **Figure 5. $\gamma\delta^{17}$ cells show higher lipid uptake and lipid droplet content**
1159 **than $\gamma\delta^{\text{IFN}}$ cells.**

1160 **(a)** Experimental set up for bulk RNA-sequencing of PLZF⁺ ($\gamma\delta^{17}$) and PLZF⁻
1161 ($\gamma\delta^{\text{IFN}}$) cells isolated from PLZF-GFP (*Zbtb16*^{GFP}) mice. **(b)** Quadrant plot of
1162 genes upregulated in tissue resident PLZF⁺ $\gamma\delta$ T cells (lower right), lymphoid
1163 PLZF⁺ $\gamma\delta$ T cells (upper left), PLZF⁺ $\gamma\delta$ T cells from all tissues (upper right) or
1164 PLZF⁻ $\gamma\delta$ T cells from all tissues (lower left). **(c)** Representative histogram of
1165 neutral lipid staining (LipidTOX) in *ex vivo* $\gamma\delta^{17}$ (CD27⁻) and $\gamma\delta^{\text{IFN}}$ (CD27⁺) cells
1166 from LNs. **(d)** LipidTOX MFI in $\gamma\delta^{17}$ and $\gamma\delta^{\text{IFN}}$ cells *ex vivo* from LNs as shown
1167 in (a) (n=11, data pooled from 3 independent experiments). **(e)** LipidTOX MFI
1168 in $\gamma\delta^{17}$ and $\gamma\delta^{\text{IFN}}$ cells from spleen, LNs, lungs, adipose, liver and skin (n=5-8,
1169 data pooled from 2 independent experiments). **(f)** Confocal imaging of $\gamma\delta^{17}$
1170 and $\gamma\delta^{\text{IFN}}$ cells expanded *in vitro* and stained with LipidTOX (red) and Hoechst
1171 33342 (blue). Scale bar represents 5 μ M (data representative of a minimum 10
1172 images from 2 independent experiments). **(g)** Quantification of confocal
1173 imaging as shown in (d) (each data point represents the average per cell per
1174 image). **(h)** Quantification of triglyceride (TAG) levels from $\gamma\delta^{17}$ and $\gamma\delta^{\text{IFN}}$ cells
1175 expanded *in vitro* (n=7, each symbol represents one biological replicate). **(i)**
1176 Filipin III staining of $\gamma\delta^{17}$ and $\gamma\delta^{\text{IFN}}$ cells *ex vivo* from LNs. Representative
1177 histogram (left) and MFI (right) (n=6, data pooled from 2 independent
1178 experiments). **(j)** Representative histogram of Bodipy-FL-C₁₆ uptake in $\gamma\delta^{17}$
1179 and $\gamma\delta^{\text{IFN}}$ cells from LNs *ex vivo* (n=8, data pooled from 2 independent
1180 experiment). **(k)** Representative plots of Bodipy-FL-C₁₆ uptake and IL-17 or
1181 IFN- γ production by $\gamma\delta^{17}$ and $\gamma\delta^{\text{IFN}}$ cells from LNs stimulated with
1182 PMA/ionomycin. **(l)** Bodipy-FL-C₁₆ MFI in IFN- γ ⁺ and IL-17⁺ $\gamma\delta$ T cells (n=4,
1183 data representative of 3 independent experiments). **(m)** Representative plot of
1184 V γ 1 and V γ 4 expression in total $\gamma\delta$ T cells and percentage Bodipy-FL-C₁₆
1185 uptake by LN $\gamma\delta$ T cell subsets (V γ 1⁺, V γ 4⁺, V γ 1⁻4⁻) (n=6, data pooled from 2
1186 independent experiment). **(n)** Representative IFN- γ and IL-17 production by
1187 V γ 4⁺ $\gamma\delta$ T cells from LNs and percentage Bodipy-FL-C₁₆ uptake by V γ 4⁺IFN- γ ⁺
1188 and V γ 4⁺IL-17⁺ $\gamma\delta$ cells (n=6, data pooled from 2 independent experiments).
1189 **(o)** Percentage Bodipy CholEsteryl FL-C₁₂ uptake by $\gamma\delta^{17}$ (CD27⁻) and $\gamma\delta^{\text{IFN}}$
1190 (CD27⁺) cells from LNs *ex vivo* (n=6, data pooled from 2 independent

1191 experiments). Error bars show mean \pm SD, * $p < 0.05$, ** $p < 0.01$, *** $p < 0.001$,
1192 **** $p < 0.0001$ using unpaired Student's t-test.

1193

1194

1195

1196 **Figure 6. High fat diet promotes the expansion of $\gamma\delta^{17}$ cells in lymph**
1197 **nodes and within tumours.**

1198 **(a)** Respiratory exchange ratio (RER) of mice fed SFD or HFD for 8 weeks
1199 (n=3, data from 1 experiment). **(b)** Bar graphs showing the percentage and
1200 absolute numbers of CD3⁺ $\gamma\delta$ T cells from LNs of standard fat diet (SFD) and
1201 high fat diet (HFD) mice (n=9, data pooled from 3 independent experiments).
1202 **(c)** Proportion of $\gamma\delta^{17}$ (CD27⁻) and $\gamma\delta^{\text{IFN}}$ (CD27⁺) T cells in LNs of SFD and
1203 HFD fed mice (n=9, data pooled from 3 independent experiments). **(d)**
1204 Percentage and absolute numbers of CD27⁺ IFN- γ ⁺ and CD27⁻ IL-17⁺ $\gamma\delta$ T
1205 cells from LNs of SFD and HFD mice (n=9, data pooled from 3 independent
1206 experiments). **(e)** Proportion of infiltrating $\gamma\delta^{17}$ cells in spleen, draining LN and
1207 tumour in the B16 tumour model (dLN and tumour n=30, data pooled from 4
1208 independent experiments, spleen n=7, naïve LN n=5). **(f)** Bar graph showing
1209 the percentage of $\gamma\delta^{17}$ and $\gamma\delta^{\text{IFN}}$ cells infiltrating tumours (n=9, data pooled
1210 from 2 experiments). **(g)** Bar graph represents the size of tumours (mm³) in
1211 SFD and HFD fed mice. **(h)** Bar graph showing proportion of infiltrating $\gamma\delta^{17}$
1212 (CD27⁻) and $\gamma\delta^{\text{IFN}}$ (CD27⁺) cells in tumours of SFD and HFD fed mice (SFD
1213 n=10, HFD n=12, data pooled from 2 independent experiments). **(i)**
1214 Representative plots of IL-17 and IFN- γ expression in $\gamma\delta$ T cells infiltrating
1215 tumours of SFD and HFD fed mice. Bar graphs represent the percentage of
1216 $\gamma\delta^{17}$ and $\gamma\delta^{\text{IFN}}$ cells infiltrating tumours (SFD n=17, HFD n=20, data pooled
1217 from 3 independent experiments). **(j)** Bar graph showing the number/mm³ of
1218 $\gamma\delta^{17}$ and $\gamma\delta^{\text{IFN}}$ cells in tumours of mice on SFD or HFD (SFD n=7, HFD n=8,
1219 data pooled from 2 independent experiments). **(k)** Plots of proliferating Ki67⁺
1220 $\gamma\delta^{17}$ cells cultured for 5h with or without cholesterol-loaded cyclodextrin (CLC).
1221 Graph represents the percentage of Ki67⁺ $\gamma\delta^{17}$ cells (data are representative

1222 of two independent experiments; pool of 3-5 mice per experiment). **(l)** $\gamma\delta^{17}$
1223 cells cultured (or not) with cholesterol-loaded cyclodextrin (CLC) for 5h were
1224 injected s.c. into E0771 tumours at d7 and d9 after tumour cell injection.
1225 Representative picture of tumours observed at day 11 post-E0771 cell
1226 inoculation. **(m)** Graph showing tumour weight at day 11 post-E0771
1227 inoculation. **(n)** E0771 tumour growth was monitored every two days after
1228 inoculation ((l-n) data are representative of three independent experiments
1229 (pool of 2-5 mice per experiment). Error bars show mean \pm SD, * $p < 0.05$,
1230 ** $p < 0.01$, *** $p < 0.001$, **** $p < 0.0001$ using unpaired Student's t-test or
1231 ANOVA test.

1232

1233 **Figure 7: Glucose supplementation enhances the effector functions of**
1234 **$\gamma\delta^{\text{IFN}}$ cells.**

1235 **(a)** Glucose uptake assessed upon i.v. injection of fluorescent 2-NBDG in
1236 tumour-bearing mice. Tumours were harvested 15 min later for analysis.
1237 Histogram represents 2-NBDG uptake in $\gamma\delta^{17}$ and $\gamma\delta^{\text{IFN}}$ cells. **(b-i)** Purified
1238 splenic and peripheral lymph nodes $\gamma\delta^{\text{IFN}}$ T cells ($\text{CD3}^+\text{TCR}\gamma\delta^+\text{CD27}^+$) were
1239 cultured in the presence of IL-7 with media containing low glucose (5mM), 2-
1240 deoxyglycose (2-DG), high glucose (50mM) or galactose (20mM) for 78h. **(b)**
1241 Plots of peripheral $\gamma\delta^{\text{IFN}}$ T cells cultured with IL-7 and media containing low
1242 glucose, 2-DG or high glucose. Histogram represents the fold change in
1243 number of $\gamma\delta^{\text{IFN}}$ T cells cultured with 2-DG or high glucose versus low glucose.
1244 **(c)** Fold change in number of proliferating Ki-67⁺ $\gamma\delta^{\text{IFN}}$ cells cultured with 2-DG
1245 or high glucose versus low glucose. **(d,e)** IFN- γ **(d)** and T-bet **(e)** expression
1246 was analysed by flow cytometry in $\gamma\delta^{\text{IFN}}$ cells incubated with media containing
1247 low glucose, 2-DG or high glucose. Histograms show the MFI of IFN- γ and T-
1248 bet. **(f)** Flow cytometry profiles of peripheral $\gamma\delta^{\text{IFN}}$ T cells cultured with IL-7 and
1249 media containing glucose (50mM) or galactose (20mM). Histogram represents
1250 the numbers of $\gamma\delta^{\text{IFN}}$ T cells. **(g,h)** IFN- γ **(g)** and T-bet **(h)** expression was
1251 analysed by flow cytometry in $\gamma\delta^{\text{IFN}}$ cells incubated with media containing
1252 glucose or galactose. Histograms show the MFI of IFN- γ and T-bet.
1253 **(i)** Representative histograms and summary of killing assay *in vitro*

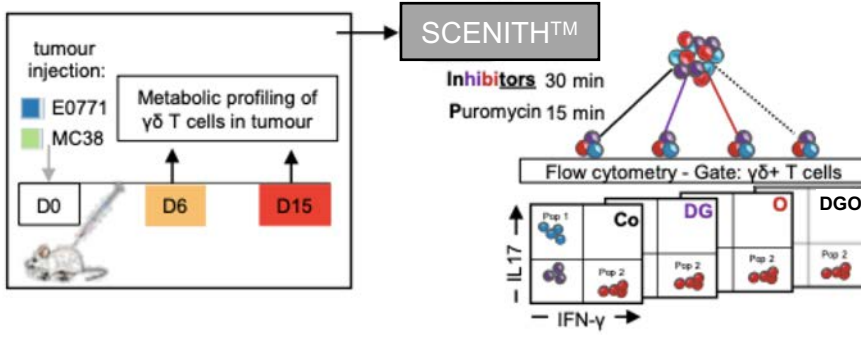
1254 of E0771 tumour cells by $\gamma\delta^{\text{IFN}}$ T cells previously supplemented (or not) with
1255 glucose (5h pre-incubation). **(j)** Representative picture of tumours observed at
1256 day 11 post-E0771 inoculation. $\gamma\delta^{\text{IFN}}$ cells supplemented (or not) with glucose
1257 for 5h were injected into the tumour at d7 and d9 after tumour cell injection.
1258 **(k)** The E0771 tumour growth was monitored every two days during 11 days
1259 after E0771 inoculation (data are representative of two **(i-k)** or four **(b-h)**
1260 independent experiments; n = 5-10 mice per group and per experiment). Error
1261 bars show mean \pm SEM, *p < 0.05, **p < 0.01, ***p < 0.001, ****p < 0.0001
1262 using unpaired Student's t-test or ANOVA test.

1263

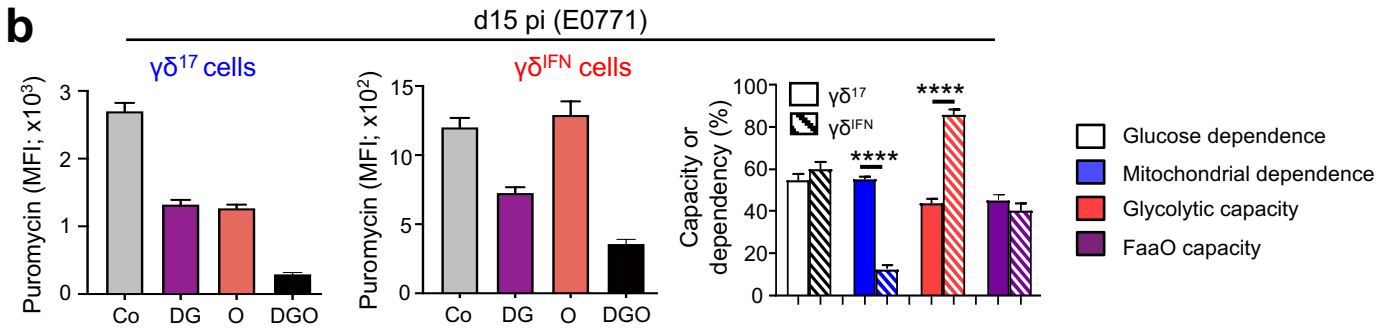
1264

Figure 1

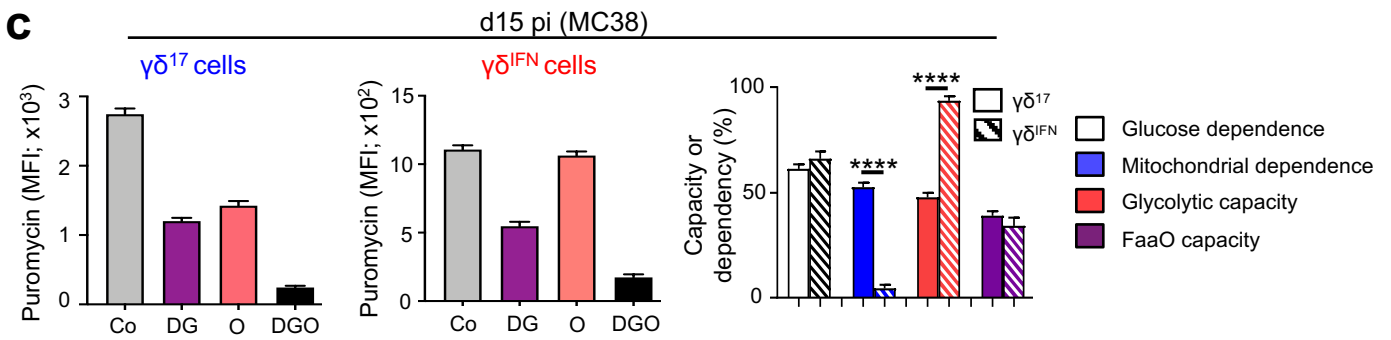
a



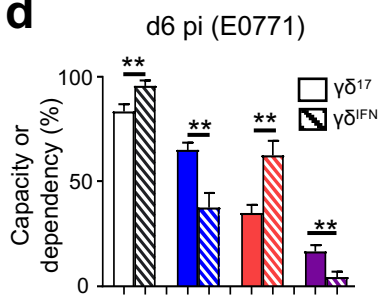
b



c



d



e

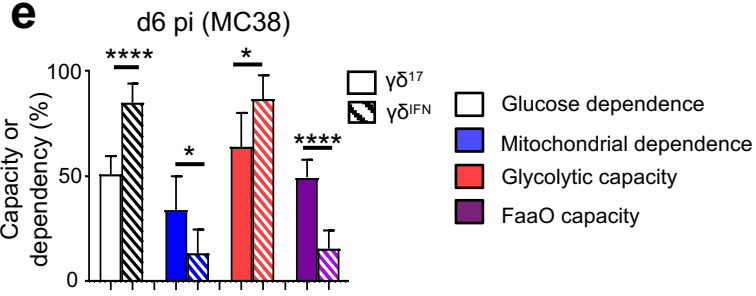


Figure 2

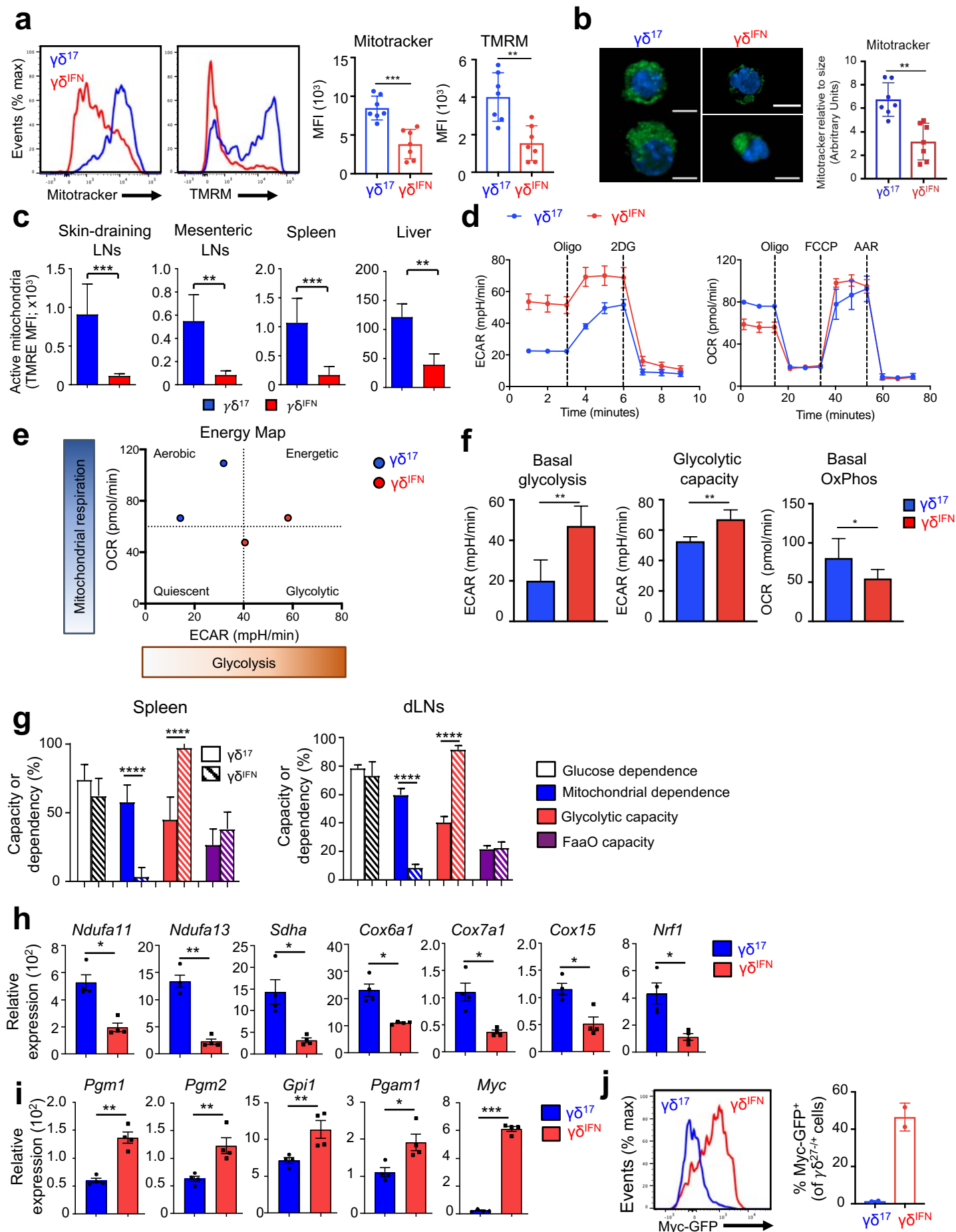
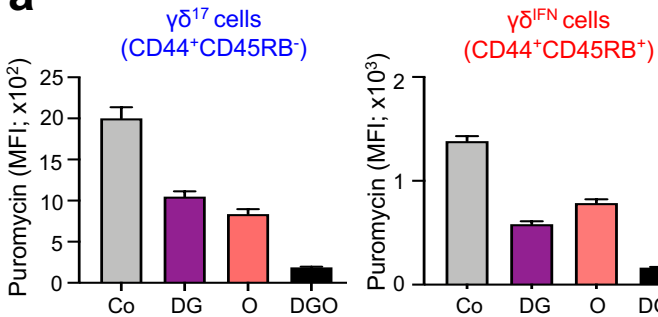
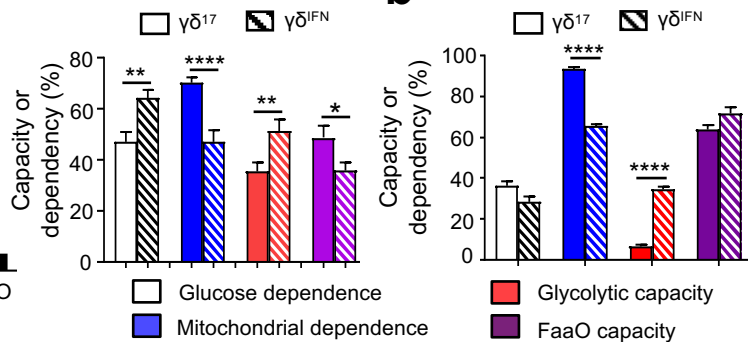


Figure 3

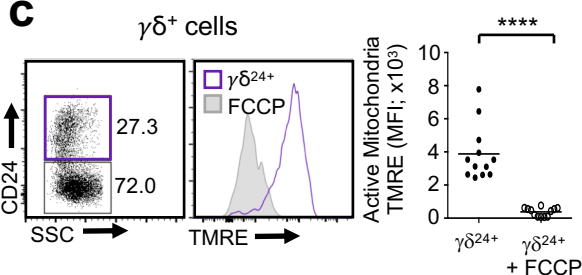
a



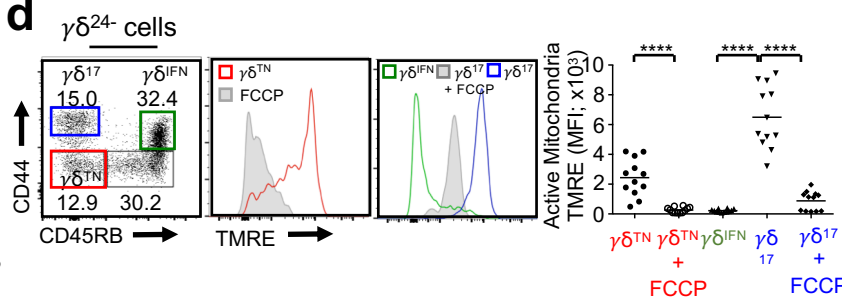
b



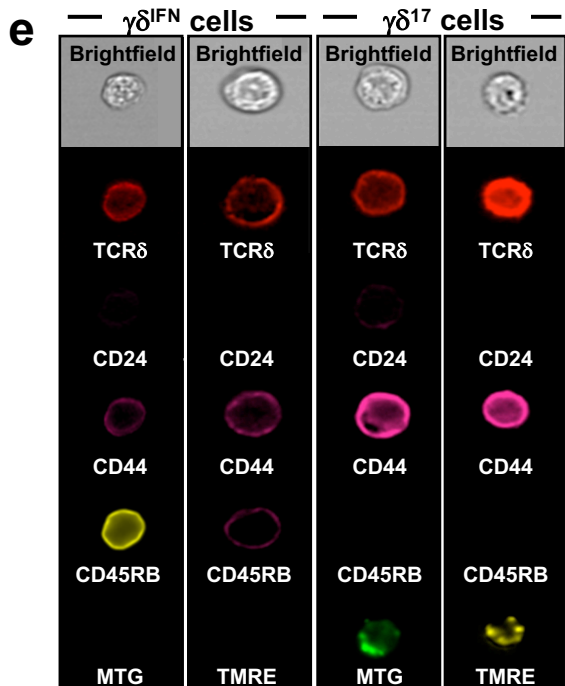
c



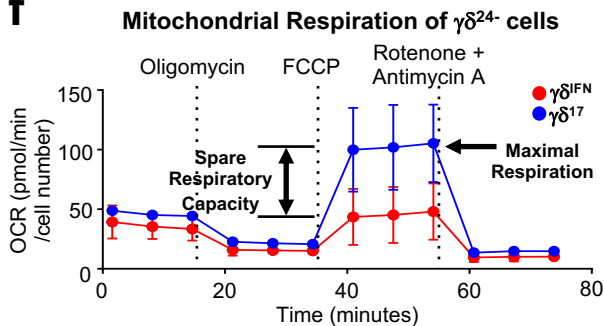
d



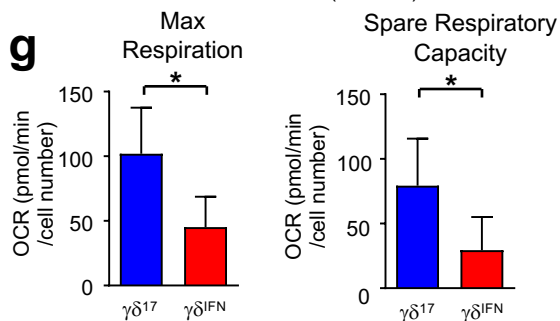
e



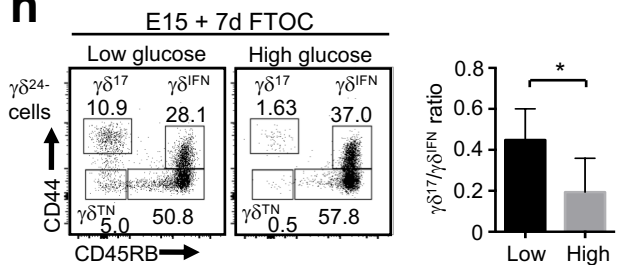
f



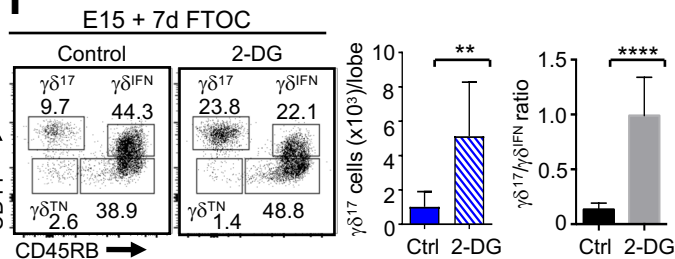
g



h



i



j

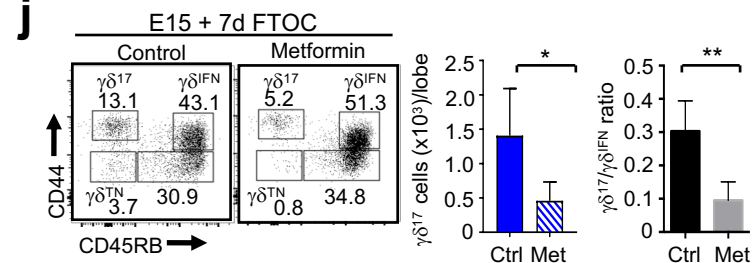


Figure 4

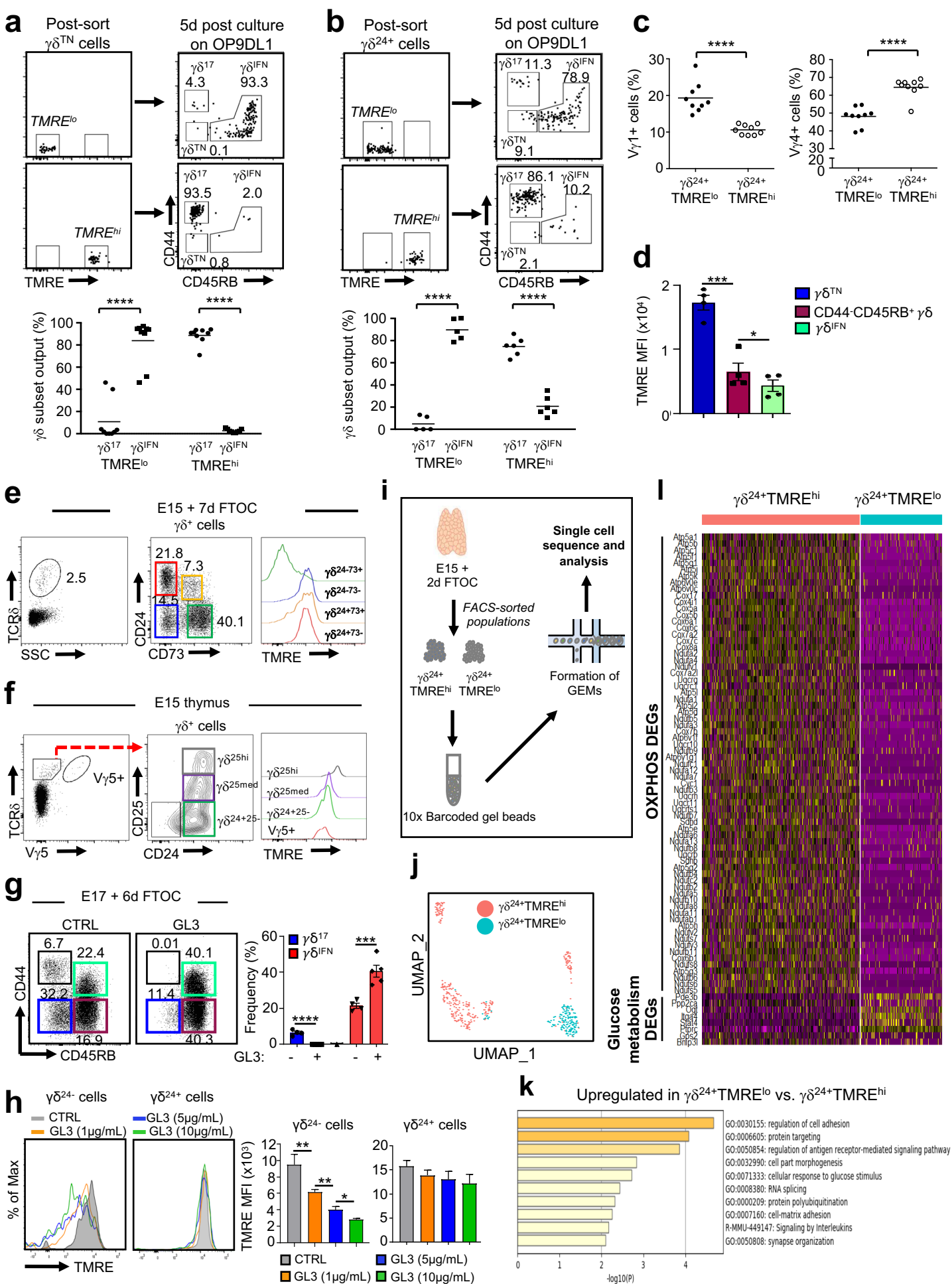


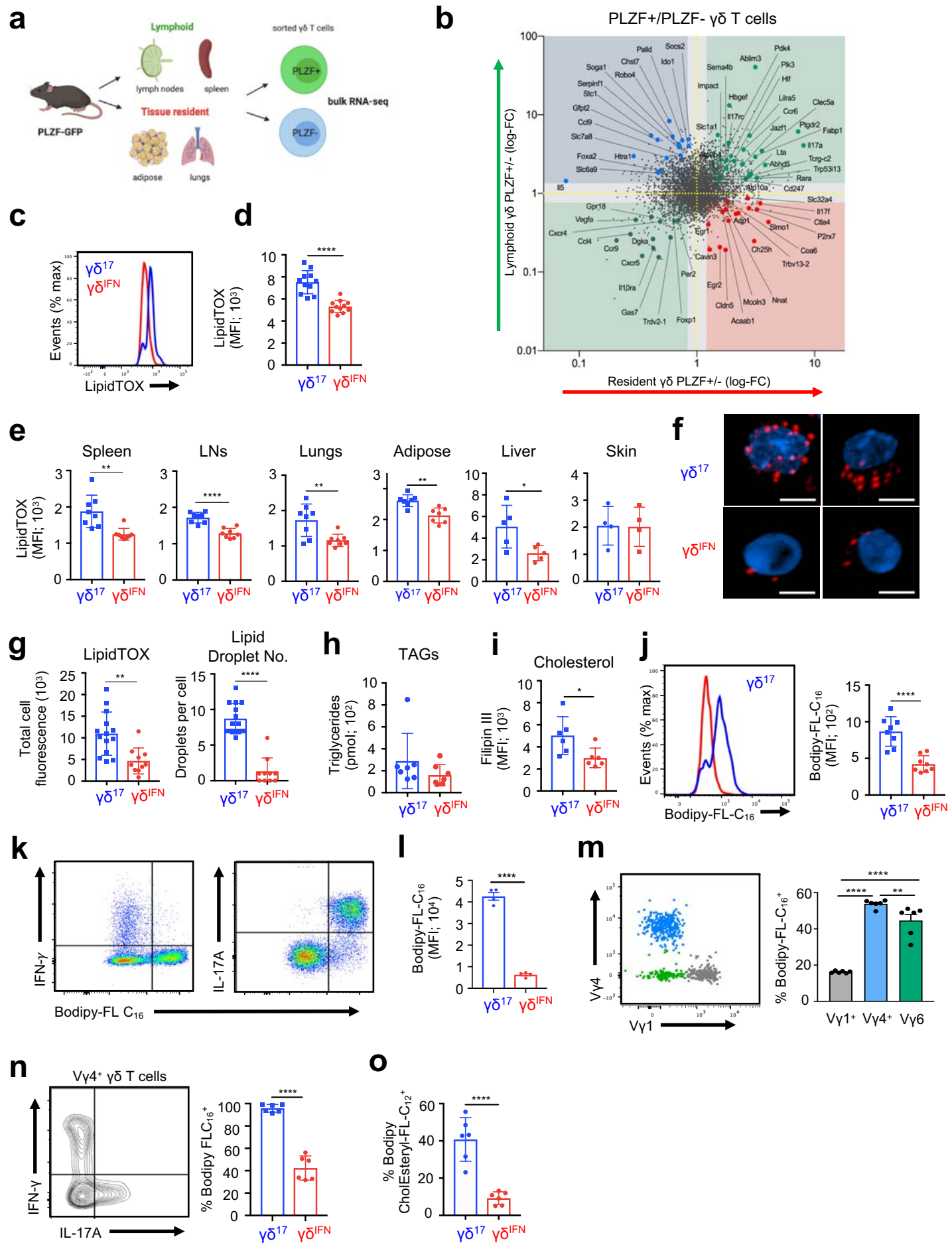
Figure 5

Figure 6

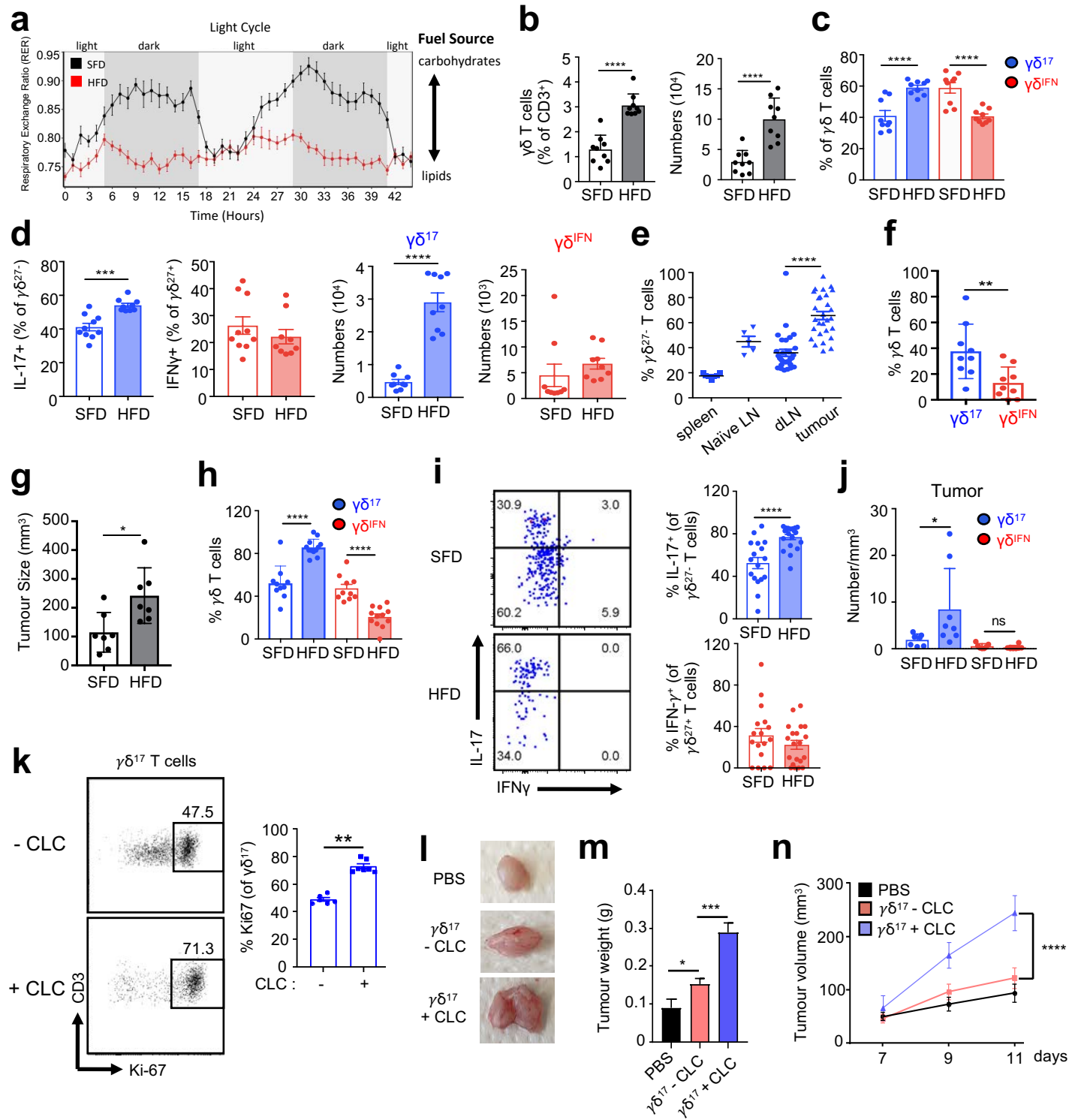


Figure 7

